

THE *CHANDRA* LOCAL VOLUME SURVEY. I. THE X-RAY POINT SOURCE POPULATIONS OF NGC 55, NGC 2403, AND NGC 4214

B. BINDER¹, B. F. WILLIAMS¹, M. ERACLEOUS², P. P. PLUCINSKY³, T. J. GAETZ³, S. F. ANDERSON¹, E. D. SKILLMAN⁴,
 J. J. DALCANTON¹, A. K. H. KONG⁵, AND D. R. WEISZ¹

¹ University of Washington, Department of Astronomy, Box 351580, Seattle, WA 98195, USA

² Department of Astronomy & Astrophysics and Center for Gravitational Wave Physics, The Pennsylvania State University,
 525 Davey Lab, University Park, PA 16802, USA

³ Harvard-Smithsonian Center for Astrophysics, 60 Garden Street, Cambridge, MA 02138, USA

⁴ University of Minnesota, Astronomy Department, 116 Church St. SE, Minneapolis, MN 55455, USA

⁵ Institute of Astronomy and Department of Physics, National Tsing Hua University, Hsinchu 30013, Taiwan

Received 2015 March 3; accepted 2015 July 6; published 2015 August 31

ABSTRACT

We present comprehensive X-ray point source catalogs of NGC 55, NGC 2403, and NGC 4214 as part of the *Chandra* Local Volume Survey. The combined archival observations have effective exposure times of 56.5 ks, 190 ks, and 79 ks for NGC 55, NGC 2403, and NGC 4214, respectively. When combined with our published catalogs for NGC 300 and NGC 404, our survey contains 629 X-ray sources total down to a limiting unabsorbed luminosity of $\sim 5 \times 10^{35} \text{ erg s}^{-1}$ in the 0.35–8 keV band in each of the five galaxies. We present X-ray hardness ratios, spectral analysis, radial source distributions, and an analysis of the temporal variability for the X-ray sources detected at high significance. To constrain the nature of each X-ray source, we carried out cross-correlations with multi-wavelength data sets. We searched overlapping *Hubble Space Telescope* observations for optical counterparts to our X-ray detections to provide preliminary classifications for each X-ray source as a likely X-ray binary, background active galactic nucleus, supernova remnant, or foreground star.

Key words: galaxies: individual (NGC 55, NGC 2403, NGC 4214) – surveys – X-rays: binaries – X-rays: galaxies

Supporting material: machine-readable and VO tables

1. INTRODUCTION

The luminous, discrete X-ray source populations ($L_X > 10^{37} \text{ erg s}^{-1}$) of inactive galaxies are dominated by X-ray binaries (XRBs; Fabbiano 2006; Fabbiano & White 2006). These are stellar systems containing an accreting compact object (either a neutron star; NS, or a black hole; BH) and a donor stellar companion, and are divided into low-mass XRBs (LMXBs) and high-mass XRBs (HMXBs) depending on the mass of the stellar companion. The donor stars of HMXBs are OB stars, while LMXBs have later type companions (usually with stellar masses $< 2 M_\odot$). Other sources of X-ray emission are also present, such as hot gas, and young supernova remnants (SNRs). Some galaxies additionally have ultraluminous X-ray sources (ULXs, $L_X > 10^{39} \text{ erg s}^{-1}$) associated with them, which are believed to be either binaries accreting at super-Eddington rates or intermediate-mass BHs. Finally, background active galactic nuclei (AGNs) are sometimes incorrectly identified as belonging to the host galaxy (Heida et al. 2013, and references therein).

Studies of XRBs and X-ray emitting SNRs in the Milky Way often suffer from significant distance uncertainties and considerable extinction along Galactic lines of sight. These difficulties are minimized, however, when studying nearby galaxies. The effects of Galactic extinction become less problematic when observing galaxies at higher Galactic latitudes, and the impact of distance uncertainties is reduced since all X-ray sources located within a particular galaxy are essentially equidistant from the observer. Therefore, observing a large number of X-ray sources in nearby galaxies can provide new insights into the characteristics of both individual X-ray sources and the global properties of the X-ray point source population.

With these considerations in mind, we undertook the *Chandra* Local Volume Survey (CLVS), a deep, volume-limited survey of five nearby galaxies (NGC 55, NGC 300, NGC 404, NGC 2403, and NGC 4214) with overlapping *Hubble Space Telescope* (*HST*) observations (down to $M_V \sim 0$; Dalcanton et al. 2009). With its excellent angular resolution ($\sim 0''.5$) and positional accuracy, *Chandra* is the best X-ray telescope for separating X-ray point source populations in nearby galaxies from the bulk of their diffuse emission. When combined with deep, optical *HST* imaging, reliable optical counterpart identification and source classification may be carried out even at distances of a few Mpc. Our collaboration has already examined the X-ray point source populations of NGC 300 (Binder et al. 2012, hereafter Paper I) and NGC 404 (Binder et al. 2013, hereafter Paper II).

The goal of the CLVS is to identify strong XRB candidates in nearby galaxies, and to compare the properties of these populations to the star formation histories (SFHs) of their host galaxies. Previous studies have shown that the fast evolutionary timescales of massive stars ($\sim 10^7$ years) makes X-ray emission from HMXBs nearly simultaneous with their formation (Grimm et al. 2003; Gilfanov et al. 2004; Shtykovskiy & Gilfanov 2007; Mineo et al. 2011, 2012), while the longer-lived LMXB systems trace older underlying stellar populations (Kong et al. 2002; Soria & Kong 2002; Trudolyubov et al. 2002); thus, the shape of the X-ray luminosity function (XLF) can be correlated with the age and SFH of the host galaxy (Grimm et al. 2003; Belczynski et al. 2004; Eracleous et al. 2006). In many of these early works, however, the current star formation rate (SFR) of the host galaxy was calculated through indirect means (i.e., $H\alpha$ luminosity, UV flux, radio

flux, etc.), and the contribution of background AGN to the XLFs could only be corrected for in a statistical sense.

By using *Chandra* to study nearby galaxies with available deep *HST* imaging, we are able to (1) directly measure both the recent and long-term SFH of each galaxy using resolved stellar populations, and (2) identify strong HMXB candidates, thereby greatly reducing the degree of contamination (from AGN, SNRs, or foreground stars) present in our XLF analysis.

In this paper, we present the X-ray point source catalogs from archival *Chandra* observations of NGC 55, NGC 2403, and NGC 4214 and compare these catalogs to those of NGC 300 and NGC 404. We describe the galaxy sample (Section 2), the archival observations and data reduction procedures (Section 3), and the methodology used to generate the X-ray source catalogs (Section 4). We then present a spectral and timing analysis of the sources in each galaxy (Section 5) and perform optical counterpart identification and X-ray source classification (Section 6).

2. GALAXY SAMPLE

The five target galaxies of the CLVS span a representative sample of disk galaxies with a range of masses, metallicities, and morphologies. When combined with the already well-studied disks of M31 (Kong & Di Stefano 2003; Williams et al. 2004; Stiele et al. 2011) and M33 (Plucinsky et al. 2008; Williams et al. 2008; Tüllmann et al. 2011), these galaxies contain $\sim 99\%$ of the stellar mass and $\sim 90\%$ of the recent star formation out to a distance of ~ 3.3 Mpc (Freedman & Madore 1988; Maíz-Apellániz et al. 2002; Tikhonov et al. 2005). Table 1 summarizes some basic properties of each galaxy included in our sample. Row (1) lists the distance (in Mpc) to each galaxy. Row (2) provides the morphological type. Rows (3) and (4) list the right ascension (R.A.) and declination (decl.), respectively (J2000.0). Row (5) provides the distance modulus to each galaxy. Row (6) provides the absolute B -magnitude. Row (7) provides the inclination angle of each galaxy, and row (8) lists the position angle (both given in degrees). Row (9) lists the major linear diameter of each galaxy, in kpc. Row (10) provides the log of the stellar mass of each galaxy, in units of M_*/M_\odot . Row (11) provides the Galactic absorbing column. Row (12) lists $12 + \log(\text{O}/\text{H})$ to give an indication of the metallicity of each galaxy. Row (13) provides the integrated (unabsorbed) 0.35–8 keV luminosity of each galaxy.

2.1. NGC 55

Along with NGC 300, NGC 55 is a member of the nearby Sculptor group of galaxies. Classified as SB(s)m type galaxy (de Vaucouleurs et al. 1991), NGC 55 is an edge-on analog of the Large Magellanic Cloud (Schmidt & Boller 1993) and is the nearest bright edge-on galaxy (Karachentsev et al. 2004). Its optical morphology is asymmetric, with a bright region displaced from the geometrical center of the galaxy (Robinson & van Damme 1966) interpreted as a bar viewed near- to end-on (de Vaucouleurs 1961). The edge-on orientation of NGC 55 offers excellent insight into the effect of disk-based star formation activity on extra-planar regions, and as such, NGC 55 has been a popular target for ISM studies (Puche et al. 1991; Ferguson et al. 1996; Hoopes et al. 1996; Otte & Dettmar 1999). Ionized gas shells are observed to protrude well above the plane of the galaxy, and at least some of this gas

appears to cool sufficiently to form new stars in the halo (Tüllmann et al. 2003; Tüllmann & Rosa 2004). The SFR derived from the total infrared luminosity of NGC 55 is $0.22 M_\odot \text{ yr}^{-1}$ (Engelbracht et al. 2004).

NGC 55 was first observed at X-ray wavelengths by *ROSAT*, revealing 15 discrete X-ray sources and localized diffuse emission within the optical confines of the galaxy (Read et al. 1997; Schlegel et al. 1997; Dahlem et al. 1998). One of these sources has been established as a ULX and likely BH-XRB (Stobbart et al. 2004). A detailed X-ray view of NGC 55 by *XMM-Newton* was presented by Stobbart et al. (2006a), with 137 X-ray sources detected within the field of view down to a flux of $\sim 5 \times 10^{-15} \text{ erg s}^{-1} \text{ cm}^{-2}$ in the 0.3–6 keV energy band. Of these sources, 42 are within the D_{25} ellipse, and the authors find ~ 20 XRB candidates, five SNRs, and seven candidate super soft sources (SSSs).

2.2. NGC 2403

NGC 2403 is an outlying member of the M81 group. Although comparable in M_B , morphology, inclination, and dynamical mass to M33, it lies more than four times farther away from M81 (the nearest large disk galaxy) than M33 is from the Milky Way (Karachentsev et al. 2002), making it a far more isolated system. NGC 2403 lacks a central bulge, but like M33 hosts a luminous compact nuclear star cluster (Davidge & Courteau 2002) containing a recently discovered X-ray transient source (Yukita et al. 2007). Additionally, NGC 2403 hosts a ULX (Swartz et al. 2004), a recent SN Type IIp (SN 2004dj, Nakano & Itagaki 2004; Beswick et al. 2005), 35 spectroscopically confirmed or suspected SNRs (Matonick et al. 1997), and 52 Wolf-Rayet candidates (Drissen et al. 1999). NGC 2403 has been observed multiple times with *XMM-Newton* (Feng & Kaaret 2005; Stobbart et al. 2006b).

The dominant age of stars within the nuclear star cluster is ~ 1.4 Gyr (Yukita et al. 2007), while numerous stars within the inner disk show stellar ages of ~ 100 Myr (Davidge & Courteau 2002). The youngest (~ 2 – 10 Myr) and most massive H II regions are 0.7–1.6 kpc from the center (Drissen et al. 1999). The global SFR of NGC 2403 is $\sim 1.2 M_\odot \text{ yr}^{-1}$ (Kennicutt 1998), and the SFH of NGC 2403 is also well measured from *HST* stellar photometry (Williams et al. 2013).

2.3. NGC 4214

Classified as an IAB(s)m similar to the Large Magellanic Cloud (de Vaucouleurs et al. 1991), NGC 4214 is one of the nearest examples of a starburst galaxy (Huchra et al. 1983; Sargent & Filippenko 1991) with a substantial population of Wolf-Rayet stars. Despite its active star formation ($\sim 0.1 M_\odot \text{ yr}^{-1}$ over the past 100 Myr; Williams et al. 2011), only a small percentage of the stellar population is young ($< 1\%$ formed in the past 50 Myr). Additionally, evidence from *HST* imaging and spectroscopy suggests the stellar initial mass function of NGC 4214 is steeper than that of Salpeter (1955) at high masses ($> 20 M_\odot$, Ubeda et al. 2007a, 2007b). Despite the elevated levels of recent star formation, however, only a small fraction of the galaxy's stars have formed since $z \sim 1$. The overall stellar populations of NGC 4214 are surprisingly similar to that of the nearby early-type dwarf galaxy NGC 404 (Williams et al. 2010).

Table 1
Summary of CLVS Galaxy Properties

	Property	NGC 55	NGC 300	NGC 404	NGC 2403	NGC 4214
(1)	Distance (Mpc)	2.1 ^a	2.0 ^b	3.05 ^b	3.3 ^c	2.9 ^c
(2)	Morphology ^d	SB(s)m	SA(s)d	SA0	SAB(s)cd	IAB(s)m
(3)	R.A. (J2000) ^e	00:14:53.6	00:54:53.5	01:09:27.0	07:36:51.4	12:15:39.2
(4)	Decl. (J2000) ^e	−39:11:48	−37:41:04	+35:43:05	+65:36:09	+36:19:37
(5)	$m - M_0^e$	26.42	26.45	27.74	27.73	27.59
(6)	M_B^d	−17.76	−17.68	−16.63	−18.61	−17.39
(7)	Inclination ^f (°)	83	45	19	56	38
(8)	Position Angle ^e (°)	108	111	0	128	0
(9)	Major linear diameter ^f (kpc)	12.05	12.95	3.25	19.43	7.05
(10)	Stellar mass ($\log(M_*/M_\odot)$)	10.48 ^d	9.63 ^g	8.83 ⁱ	10.27 ^j	9.18 ^f
(11)	N_H ^k (10^{20} cm^{-2})	1.37	4.19	5.13	4.36	1.99
(12)	$12 + \log(\text{O}/\text{H})$	8.05 ^l	8.41 ^m	8.6 ⁿ	8.48 ^o	8.36 ^p
(13)	total unabs. $\log(L_X)$ (erg s^{-1} , 0.35–8 keV)	39.34 ^q	38.49 ^q	37.85 ^r	40.23 ^s	38.87 ^t

Notes.

^a Tikhonov et al. (2005), ^b Dalcanton et al. (2009), ^c Freedman & Madore (1988), ^d de Vaucouleurs et al. (1991), ^e NED, ^f Karachentsev et al. (2004), ^g Muñoz-Mateos et al. (2007), ^h Puche et al. (1990), ⁱ Thilker et al. (2010), ^j de Blok et al. (2008), ^k Column density through the ISM of the Milky Way (Kalberla et al. 2005), ^l Lee et al. (2006), ^m Bresolin et al. (2009), ⁿ Bresolin (2013), ^o Berg et al. (2013), ^p Engelbracht et al. (2008), ^q Zang et al. (1997), ^r Komossa et al. (1999), ^s Fraternali et al. (2002), ^t Ott et al. (2005).

NGC 4214 was the host of a SN Ia (Wellmann 1955) and a recent nova (Humphreys et al. 2010). The most luminous X-ray source in NGC 4214, CXOU J121538.2+361921, is an XRB with a 3.62 hr period and is likely composed of a slightly evolved He-burning donor (of $\sim 2\text{--}3 M_\odot$) and a NS (Dewi 2006; Ghosh et al. 2006). The X-ray point source population of NGC 4214 was investigated using both *Chandra* and *XMM-Newton* observations by Hartwell et al. (2004), who demonstrated that the high energy properties of NGC 4214 were comparable to other dwarf starbursts down to a limiting luminosity of $\sim 10^{36} \text{ erg s}^{-1}$.

3. OBSERVATIONS AND DATA REDUCTION

3.1. Observations and Image Alignment

We constructed the X-ray point source catalogs of NGC 55, NGC 2403, and NGC 4214 using archival *Chandra* ACIS data. All data reduction used CIAO v4.3 and CALDB v4.4.2 using standard reduction procedures. All observations were reprocessed from evtl level files using the CIAO routine `acis_process_events`. The data were corrected for bad pixels/columns, charge transfer inefficiency, time-dependent gain variations, and the pixel randomization was removed. The event list was restricted to the pipeline-provided good time intervals, grades = 0, 2, 3, 4, 6, and status = 0. Background light curves were generated from source-free event lists for each observation, and a sigma-clipping algorithm was applied to remove time intervals with count rates more than 5σ from the mean. Exposure maps and exposure-corrected images were made using `fluximage` and observations were then merged using `reproject_image`.

Spectral weights used for the instrument maps were generated assuming a power law spectrum with $\Gamma = 1.9$ (appropriate for both XRBs and background AGN) and the foreground hydrogen column density provided in Table 1. Since many background AGN (and XRBs) show evidence for absorption beyond that of the Galactic column (see Section 5.2 for further discussion of these sources), we generated spectral weights assuming a highly absorbed power law (with $\Gamma = 1.9$

but N_H an order of magnitude larger than the Galactic value). From the resulting instrument and exposure maps, we found that the assumption of Galactic absorption will lead to a flux overestimation in sources that are intrinsically more absorbed: the predicted unabsorbed fluxes differ by $\sim 35\%$ in the 0.5–2 keV band and $\sim 5\%$ in the 2–8 keV band.

Table 2 summarizes the archival observations used in this work. Column (1) lists the galaxy. Column (2) provides the *Chandra* observation IDs. Column (3) lists the date on which each observation was performed. Column (4) gives the usable exposure time acquired during each observation from the sigma-clipping algorithm, and column (5) lists this time as a fraction of the total exposure. Columns (6) and (7) provide the R.A. and decl. (J2000.0) of the *Chandra* aim-point. Column (8) lists the detector used during each observation.

3.2. Image Alignment

A total of 13 *HST* fields were used to search for optical counterparts for each X-ray source: six fields in NGC 55, five in NGC 2403, and two in NGC 4214. The *HST* fields were selected from the ACS Nearby Galaxy Survey Treasury; details of the *HST* data acquisition and reduction are provided in Dalcanton et al. (2009). In the case of NGC 2403, three of the five *HST* fields targeted the halo and were far off the nominal *Chandra* aim-points.

To identify candidate optical counterparts to the *Chandra* X-ray sources, both the *Chandra* and *HST* fields need to be placed onto a common, reference coordinate frame. We place all observations (X-ray and optical) onto the International Celestial Reference System (ICRS) by finding matches (within $\sim 5''$) between stars or background galaxies in the 2MASS Point Source Catalog (Skrutskie et al. 2006). We were able to identify between three and six bright 2MASS sources per field which matched either a *Chandra* X-ray source, optical foreground star, or background galaxy. The plate solutions were computed using the IRAF task `cmap`, with rms residuals from the ICRS frame typically less than a few hundredths of an arcsecond in both R.A. and decl. The total alignment error applied to the coordinates of each X-ray source was computed by summing the *Chandra* and

Table 2
Summary of *Chandra* Observations

Galaxy	Observation ID	Date	Effective Exposure Time (ks)	Fraction of Total Exposure Time	R.A. ^a (J2000)	Decl. ^a (J2000)	Detector
(1)	(2)	(3)	(4)	(5)	(6)	(7)	(8)
NGC 55	2255	2001 Sep 11	47	78.6%	00:15:08.5	−39:13:13.3	ACIS-I
	4744	2004 Jun 29	9.5	99.7%	00:14:54.0	−39:11:49.0	ACIS-I
	Total	...	56.5	82.5%
NGC 2403	2014	17 Apr 2001	35	98.8%	07:36:51.9	+65:36:00.6	ACIS-S
	4627	2004 Aug 9	31	75.6%	07:37:17.1	+65:35:58.3	ACIS-S
	4628	2004 Aug 23	42	89.7%	07:37:17.1	+65:35:58.3	ACIS-S
	4629	2004 Oct 3	40	90.9%	07:37:17.1	+65:35:58.3	ACIS-S
	4630	2004 Dec 22	42	86.5%	07:37:17.1	+65:35:58.3	ACIS-S
	Total	...	190	88.4%
NGC 4214	2030	2001 Oct 16	25	96.2%	12:15:38.7	+36:19:41.9	ACIS-S
	4743	2004 Apr 3	26	96.3%	12:15:38.9	+36:19:40.0	ACIS-S
	5197	2004 July 30	28	98.6%	12:15:38.9	+36:19:40.0	ACIS-S
	Total	...	79	97.5%

Note.

^a Observation coordinates are those of the *Chandra* ACIS aim-point.

HST rms residuals in quadrature. For both NGC 2403 and NGC 4214, two of the available *HST* fields overlapped with one another; we were able to identify one source in NGC 2403 that was suitable for alignment in both the *HST* fields, and two sources in the overlap region of NGC 4214.

Figure 1 shows the 2MASS *J*-band image of NGC 55 and ground-based *r*-band images of NGC 2403 and NGC 4214. The positions of discrete X-ray sources are shown in red. Only the two *HST* fields covering the NGC 2403 disk are shown, as the remaining three fields targeted the galaxy’s halo and contain only a small number of X-ray sources.

A summary of our *HST* observations and the results of our astrometry are provided in Table 3. Column (1) lists the galaxy name. Column (2) provides a description of the field (e.g., “*Chandra*” for the X-ray image, “DISK” for the archival *HST* field labeled “disk”) and column (3) provides the corresponding *HST* observation IDs. Column (4) lists the number of X-ray sources contained within each field. Columns (5) and (6) provide the R.A. and decl. (J2000.0) of the telescope aim-points. Column (7) lists the number of sources used to align the field to the ICRS. Columns (8) and (9) provide the rms uncertainty in the R.A. and decl., respectively. Overall, these uncertainties are smaller than the individual source position uncertainties. Thus, our counterpart analysis was limited by the uncertainties in the X-ray source centroids.

4. X-RAY SOURCE CATALOGS

4.1. Catalog Creation

For consistency with Papers I and II, we employed the same iterative source detection strategy (developed by Tüllmann et al. 2011). A summary of the approach is given here, and the reader is referred to Papers I and II for further details. The CIAO task *wavdetect* (Freeman et al. 2002) was used to create a list of source candidates; *wavdetect* was run on each individual exposure for each galaxy and on the stacked image. These source candidates were used as input to ACIS-Extract (AE; Broos et al. 2010). AE is a source extraction and characterization tool which was used to determine various

source properties (source and background count rates, detection significances, fluxes, etc.) and to generate light curves and spectra with appropriate response matrices. The Poisson probability of not being a source (*prob_no_source*; hereafter *pns*) provided by AE (Weisskopf et al. 2007, Appendix A2) was used to select highly significant sources for inclusion in the X-ray source catalogs. The *pns* value provides the Poisson probability that all of the counts in the source extraction region are actually from the background (in the given energy band); therefore, candidate sources with low *pns* values are most likely to be genuine.

For each input source, AE creates background regions by first removing all sources from the data and then searching for the smallest circular region around each source that encompasses at least 50 counts (changing the number of background counts required does not significantly affect source properties; Tüllmann et al. 2011). These background regions are used to extract background spectra. To extract the X-ray spectrum for each source, AE constructs a polygon region that approximates the 90% contour of the *Chandra*-ACIS PSF at the location of the source. The CIAO tools *mkacisrmf* and *mkarf* are used to create appropriate response and ancillary response matrices, respectively, for each source.

The initial source lists generated by *wavdetect* were deliberately constructed to include many more sources than we anticipated being statistically significant. Each source list was then filtered to remove spurious sources and improve source and background regions following the iterative procedure of Papers I, II, and Tüllmann et al. (2011). Both the construction of the initial source list and all subsequent iterations with AE were run on the combined images for each galaxy (e.g., using all available exposures, to ensure detection of faint sources). For our final iteration with AE, we required that a candidate X-ray source have $pns < 4 \times 10^{-6}$ (Nandra et al. 2005; Georgakakis et al. 2008; Tüllmann et al. 2011) in any of the following energy bands: 0.5–8, 0.5–2, 2–8, 0.5–1, 1–2, 2–4, 4–8, 0.35–1, or 0.35–8 keV. If we would have considered only the 0.35–8.0 keV band, ~4–8% of significant sources would have been missed.

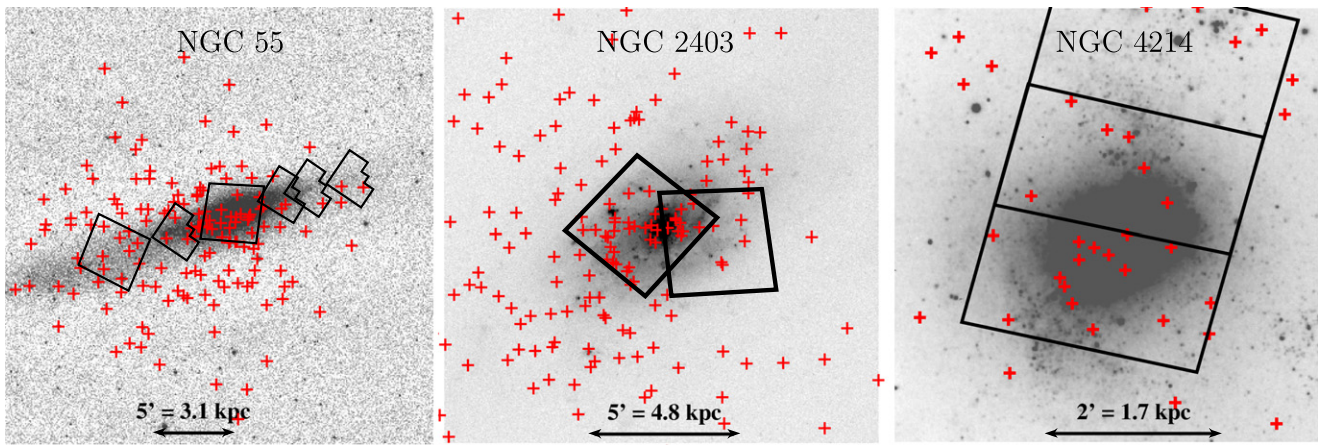


Figure 1. Images of NGC 55 (left, 2MASS *J*-band), NGC 2403 (middle, ground-based *r*-band), and NGC 4214 (right, ground-based *r*-band). Highly significant discrete point sources (i.e., those with $pns < 4 \times 10^{-6}$) are shown as red crosses. *HST* fields are shown in black.

Table 3
Alignment of *Chandra* and *HST* Images to 2MASS

Galaxy	Description	<i>HST</i> Obs. ID	# of X-ray Sources in Field	R.A. (J2000)	Decl. (J2000)	# Sources Used For Alignment	rms, R.A. ^a	rms, Decl. ^a
(1)	(2)	(3)	(4)	(5)	(6)	(7)	(8)	(9)
NGC 55	<i>Chandra</i>	merged	154	00:15:09.96	−39:13:12.9	5	0″0297	0″0942
	WIDE-1	11307	2	00:14:16.54	−39:09:45.0	4	0″0783 (0″0725)	0″2265 (0″2060)
	WIDE-3	11307	1	00:14:30.03	−39:10:18.8	4	0″0533 (0″0443)	0″1174 (0″0701)
	WIDE-4	11307	3	00:14:38.26	−39:10:41.9	4	0″0401 (0″0270)	0″2437 (0″0877)
	WIDE-5	11307	4	00:15:11.55	−39:12:58.3	4	0″3832 (0″3820)	0″1197 (0″0740)
	DISK	9765	9	00:15:31.06	−39:14:13.4	5	0″0323 (0″0126)	0″1262 (0″0840)
	FIELD	9765	22	00:14:53.73	−39:11:48.1	6	0″0454 (0″0343)	0″1301 (0″0898)
NGC 2403	<i>Chandra</i>	merged	190	07:37:12.85	+65:36:21.0	4	0″0048	0″0296
	HALO-1	10523	1	07:37:54.67	+65:31:29.2	4	0″0127 (0″0118)	0″0636 (0″0563)
	HALO-6	10523	8	07:37:31.38	+65:40:29.5	6	0″0569 (0″0567)	0″0412 (0″0287)
	HALO-7	10523	2	07:38:01.5	+65:43:49.1	4	0″0098 (0″0086)	0″0473 (0″0369)
	X-1	10579	18	07:36:42.36	+65:35:36.3	4	0″0069 (0″0050)	0″0419 (0″0296)
	PR	10182	37	07:36:58.6	+65:36:10.9	3	0″0702 (0″0700)	0″0487 (0″0387)
NGC 4214	<i>Chandra</i>	merged	116	12:15:39.51	36:17:22.6	4	0″0101	0″0541
	N4214	11986	4	12:15:32.63	36:21:40.7	3	0″0147 (0″0108)	0″0541 (0″0012)
	DEEP	10915	4	12:15:23.22	36:21:51.9	4	0″0134 (0″0088)	0″0566 (0″0166)

Note.

^a Alignment errors listed show the uncertainties in each individual field and the *Chandra* image added in quadrature. The error in parentheses is the uncertainty reported by *ccmap* for the individual fields.

Using a pns threshold of 4×10^{-6} results in ~ 0.5 false source detections per megapixel (determined by e.g., Nandra et al. 2005; Georgakakis et al. 2008). There is approximately one megapixel per ACIS CCD, and source detection was performed in nine separate energy bands. Thus, we calculate the number of false positives in our catalogs as $0.5 \times 9 \times$ the number of CCDs used in the source detection process. NGC 55 was observed with ACIS-I (4 CCDs), while NGC 2403 and NGC 4214 were observed with ACIS-S (with source detection performed on S2-4 in both cases). We therefore expect ~ 18 , 14, and 14 false sources to be present in the X-ray source catalogs of NGC 55, NGC 2403, and NGC 4214, respectively. Of the 629 X-ray sources detected at high significance across all five galaxies, $\sim 94\%$ have fewer than 200 net counts. Half of all X-ray sources have error circles smaller than $2''$ in radius and 54% have off-axis angles less than $5'$.

Table 4 summarizes the number of candidate X-ray sources included in the source lists for each CLVS galaxy at each step in our iterative source detection procedure. Column (1) lists the galaxy. Column (2) lists the number of sources contained in the original *wavdetect* source list. Column (3) provides the number of sources remaining after our first pass through AE. Column (4) lists the number of sources remaining after the second pass through AE, and column (5) lists the number of sources in the final source catalog.

The final source catalogs for NGC 55, NGC 2403, and NGC 4214 contain 154, 190, and 116 X-ray sources, respectively, and 95 and 74 sources for earlier studies of NGC 300 and NGC 404, respectively. A total of 629 highly significant X-ray sources were detected as part of the CLVS.⁶ The remainder of

⁶ Complete source catalogs for all five CLVS galaxies are available in FITS format at <http://www.astro.washington.edu/users/bbinder/CLVS/>.

Table 4
Number of X-ray Sources at each AE Iteration

Galaxy (1)	Initial (2)	First Pass (3)	Second Pass (4)	Final (5)
NGC 55	906	370	220	154
NGC 300	799	224	126	95
NGC 404	762	129	104	74
NGC 2403	1308	648	298	190
NGC 4214	1177	474	211	116
Total	4952	1845	959	629

this work utilizes these highly significant sources. However, it is possible that some marginally detected sources (i.e., those sources that failed to meet our final *pns* requirement) are in fact genuine X-ray sources, and other observers may wish to use different source selection criteria than we employed here. The locations of the lower-significance sources have been excluded in Figure 1, where there exist a handful of regions showing evidence for X-ray emission but an X-ray point source was not identified. In these regions, either the X-ray emission was too diffuse to be categorized as a point source (and therefore failed to be included in our catalog), or the X-ray source failed to meet our *pns* criteria of $<4 \times 10^{-6}$. For that reason, we additionally release an expanded version of each X-ray source catalog, where X-ray sources are required only to meet a *pns* threshold of 10^{-3} .

The positions and properties of the sources in the expanded X-ray point source catalogs (for all five CLVS galaxies) are listed in Table 5. Column (1) provides a unique X-ray ID number, with the highly significant sources listed first according to increasing R.A. (J2000.0), followed by the marginally detected (and mostly spurious) sources (marked with an asterisk). Column (2) provides the source catalog name, using R.A. and decl. nomenclature. Columns (3)–(4) provide the R.A. and decl., respectively (J2000.0). Column (5) provides the positional uncertainty of the X-ray sources, in arcseconds. Column (6) lists the off-axis angle from the nominal *Chandra* aim-point, in arcminutes. For sources that were detected during multiple *Chandra* observations, the minimum off-axis angle is reported. Column (7) provides the net counts detected in the 0.35–8 keV energy band for all available *Chandra* observations. Column (8) provides the log of 0.35–8 keV *pns* value for each source.⁷ Column (9) provides the unabsorbed 0.35–8 keV flux predicted for each source, assuming a power law spectrum with $\Gamma = 1.9$ and absorption due to the Galactic column only.

4.2. Sensitivity Maps

The remainder of the analyses in this work require sensitivity maps, which provide the energy flux level at which a source could be detected for each point in our survey area. We convert the AE-provided photon flux for each source (*flux2*, which is based on the net source counts, exposure time, and the mean auxiliary response file (ARF) in the given energy band) into energy fluxes assuming a power law with $\Gamma = 1.9$ that is absorbed by the appropriate Galactic column density for each galaxy. Since the majority of X-ray sources in each catalog are either XRBs or background AGN, we expect this model to be

appropriate and not to systematically bias our subsequent analyses.

To create sensitivity maps, we calculated the number of source counts that would be required to meet our *pns* criteria ($<4 \times 10^{-6}$) for each point in the survey area, following Georgakakis et al. (2008). The limiting fluxes (and corresponding luminosities) in the 0.35–8, 0.5–2, and 2–8 keV bands for each galaxy are summarized in Table 6. Column (1) lists the galaxy and column (2) lists the energy band, in keV, being considered. Columns (3) and (4) provide the fluxes and corresponding luminosities to which 70% of the survey area is complete, respectively. Columns (5) and (6) provide the fluxes and corresponding luminosities to which 90% of the survey area is complete, respectively. Columns (7) and (8) provide the fluxes and corresponding luminosities to which 95% of the survey area is complete, respectively. Columns (9) and (10) list the flux and luminosity, respectively, of the faintest source that met the *pns* threshold to be included in our catalogs. All fluxes are reported in units of 10^{-15} erg s $^{-1}$ cm $^{-2}$, and all luminosities are in units of 10^{36} erg s $^{-1}$.

5. THE X-RAY POINT SOURCE POPULATIONS

The X-ray properties of individual sources, such as their spectral shape and temporal variability, can be used to constrain the physical origin of the X-ray emission. Additionally, bulk population properties (such as the radial distribution of sources) enable us to identify different X-ray populations statistically. We expect the X-ray point source populations of NGC 55, NGC 2403, and NGC 4214 to consist of HMXBs, LMXBs, SNRs, background AGN, and foreground stars. We use our X-ray point source catalogs to search for time-variable sources, analyze hardness ratios (HRs) (for faint sources) and perform spectral fitting (for bright sources), and construct radial source distributions. In a follow-up paper, we consider the properties of the source populations in more depth, and discuss the implications of our data for scenarios of HMXB evolution.

5.1. Hardness Ratios

The X-ray spectrum of a source can provide a key diagnostic for separating different populations. However, it is not reliably possible to constrain spectral parameters to any degree of accuracy for sources with $\lesssim 50$ counts. The majority of the CLVS X-ray sources fall within this low-count regime.

Instead of directly measuring the X-ray spectral shape, we define hardness ratios (HRs, also called X-ray colors) to separate different populations. HRs measure the fraction of photons emitted by a source in different energy ranges. We use the following energy bands in our analysis: soft (*S*, 0.35–1.1 keV), medium (*M*, 1.1–2.6 keV), and hard (*H*, 2.6–8 keV). We evaluate two HRs for each source using the same approach as in Papers I and II. Source and background counts were determined by AE in each band, and we define a “soft” color,

$$\text{HR1} = \frac{M - S}{H + M + S}, \quad (1)$$

⁷ Although Table 5 only lists the *pns* value in the 0.35–8 keV band, *pns* values in all energy bands will be included in the FITS catalogs.

Table 5
Expanded X-ray Source Lists for All Galaxies in the *Chandra* Local Volume Survey

Source No.	Source ID (CXOLV J+...)	R.A. (J2000)	Decl. (J2000)	Positional Error (")	θ^a (')	Net Counts (0.35–8 keV)	$\log(pns)$ (0.35–8 keV)	$f_{0.35-8\text{ keV}}^b$ (10^{-15} erg s $^{-1}$ cm $^{-2}$)
(1)	(2)	(3)	(4)	(5)	(6)	(7)	(8)	(9)
NGC 300								
1	005411.98-373951.8	13.5499370	−37.664408	0.70	8.2	22.8 $^{+6.6}_{-5.5}$	−9.1	4.0
2	005412.31-373359.6	13.5513190	−37.566583	0.93	9.3	18.2 $^{+6.6}_{-5.5}$	−4.8	3.4
3	005413.98-373710.5	13.5582680	−37.619588	0.36	7.9	70.8 $^{+9.8}_{-8.8}$	<−10	12.4
4	005415.57-373316.4	13.5649070	−37.554563	0.59	9.2	45.1 $^{+8.5}_{-7.4}$	<−10	11.8
5	005419.92-373744.5	13.5830010	−37.629032	0.61	6.6	12.1 $^{+5.0}_{-3.8}$	−6.0	2.0
6	005421.10-374241.2	13.5879360	−37.711458	0.51	7.5	31.1 $^{+7.1}_{-6.0}$	<−10	6.4
7	005422.16-374024.6	13.5923720	−37.673501	0.67	6.3	9.4 $^{+4.7}_{-3.6}$	−3.8	1.5
8	005422.52-374312.1	13.5938400	−37.720045	0.59	7.5	22.5 $^{+6.4}_{-5.3}$	<−10	3.9
9	005422.52-373850.6	13.5938410	−37.647406	0.45	6.0	16.1 $^{+5.5}_{-4.3}$	−9.0	2.7
10	005425.06-374358.2	13.6044550	−37.732836	0.53	7.6	29.4 $^{+7.1}_{-6.0}$	<−10	5.4
NGC 404								
1	010838.25+354027.3	17.1593960	35.674264	0.23	10.0	655.3 $^{+27.2}_{-26.1}$	<−10	95.3
2	010841.45+354056.8	17.1727100	35.682458	0.47	9.3	116.5 $^{+13.1}_{-12.0}$	<−10	13.2
3	010842.38+354300.8	17.1765910	35.716903	0.55	8.9	67.4 $^{+10.6}_{-9.5}$	<−10	7.8
4	010847.72+353948.3	17.1988680	35.663419	0.69	8.4	33.2 $^{+8.3}_{-7.2}$	−9.5	3.7
5	010848.00+354437.4	17.2000240	35.743725	0.37	7.9	34.2 $^{+7.1}_{-6.0}$	<−10	12.3
6	010848.45+354433.4	17.2018810	35.742616	0.37	7.8	37.5 $^{+7.4}_{-6.3}$	<−10	10.1
7	010848.48+353906.9	17.2020350	35.651937	0.22	8.5	454.3 $^{+22.8}_{-21.8}$	<−10	51.6
8	010850.31+353843.8	17.2096470	35.645503	0.60	8.3	46.0 $^{+9.1}_{-8.0}$	<−10	5.1
9	010853.61+354501.9	17.2234150	35.750537	0.58	6.9	26.2 $^{+6.8}_{-5.7}$	<−10	4.2
10	010854.69+354239.7	17.2279010	35.711041	0.41	6.4	40.0 $^{+7.9}_{-6.8}$	<−10	4.2
NGC 55								
1	001503.50-391533.8	3.7645870	−39.259401	0.19	2.7	9.8 $^{+4.3}_{-3.1}$	<−10	1.6
2	001502.09-391646.1	3.7587260	−39.279490	0.25	3.9	11.6 $^{+4.6}_{-3.4}$	<−10	2.1
3	001458.59-392211.3	3.7441560	−39.369828	0.45	9.2	81.1 $^{+10.7}_{-9.6}$	<−10	15.0
4	001459.11-391901.6	3.7463080	−39.317128	0.47	6.4	18.7 $^{+5.7}_{-4.6}$	<−10	2.8
5	001459.34-391723.1	3.7472760	−39.289762	0.23	4.8	30.0 $^{+6.6}_{-5.5}$	<−10	4.3
6	001502.18-391425.2	3.7591020	−39.240335	0.17	1.9	7.9 $^{+4.0}_{-2.8}$	<−10	2.9
7	001451.70-392417.8	3.7154570	−39.404951	0.62	11.6	103.3 $^{+12.2}_{-11.1}$	<−10	20.7
8	001448.96-392229.9	3.7040110	−39.374988	0.38	10.1	168.6 $^{+14.5}_{-13.5}$	<−10	33.0
9	001457.84-391555.7	3.7410040	−39.265498	0.20	3.7	17.4 $^{+5.3}_{-4.2}$	<−10	2.6
10	001500.62-391414.2	3.7525970	−39.237285	0.18	2.2	3.0 $^{+2.9}_{-1.6}$	−5.2	1.1
NGC 2403								
1	073706.49+652736.5	114.2770800	65.460154	0.72	8.2	30.0 $^{+8.3}_{-7.2}$	−6.7	3.8
2	073707.39+653455.8	114.2808300	65.582175	0.02	1.9	904.7 $^{+31.1}_{-30.1}$	<−10	31.4
3	073705.08+653146.7	114.2711900	65.529650	0.21	4.5	54.9 $^{+8.9}_{-7.8}$	<−10	3.5
4	073701.86+652751.6	114.2577900	65.464334	0.82	8.0	22.2 $^{+7.3}_{-6.2}$	−5.2	3.1
5	073707.11+653515.8	114.2796600	65.587735	0.16	1.6	8.7 $^{+4.3}_{-3.1}$	−5.7	0.5
6	073703.99+653241.6	114.2666600	65.544909	0.37	3.6	10.8 $^{+4.6}_{-3.4}$	−6.9	1.4
7	073706.42+653451.8	114.2767500	65.581057	0.08	1.9	41.5 $^{+7.7}_{-6.6}$	<−10	1.4
8	073701.68+653236.3	114.2570200	65.543435	0.27	3.8	20.3 $^{+6.2}_{-5.1}$	−8.0	0.9
9	073656.80+653029.4	114.2366800	65.508181	0.29	5.8	82.2 $^{+11.2}_{-10.1}$	<−10	5.6
10	073659.27+653149.7	114.2469800	65.530482	0.29	4.5	36.4 $^{+7.9}_{-6.8}$	<−10	2.3
NGC 4214								
1	121537.80+361613.2	183.9075100	36.270343	0.41	3.7	7.0 $^{+4.0}_{-2.8}$	−4.7	2.0
2	121531.56+360947.4	183.8815200	36.163172	0.92	9.2	28.3 $^{+7.6}_{-6.4}$	−8.1	5.5
3	121533.96+361428.5	183.8915300	36.241258	0.36	3.1	5.8 $^{+3.6}_{-2.4}$	−7.1	1.8
4	121530.29+361203.6	183.8762200	36.201004	0.39	5.6	32.7 $^{+6.9}_{-5.8}$	<−10	10.6
5	121533.02+361531.2	183.8876100	36.258681	0.37	4.2	19.8 $^{+6.0}_{-4.9}$	−9.3	2.5
6	121524.05+361252.1	183.8502100	36.214481	0.69	5.5	8.7 $^{+4.3}_{-3.1}$	−5.7	3.4

Table 5
(Continued)

Source No.	Source ID (CXOLV J+...)	R.A. (J2000)	Decl. (J2000)	Positional Error (")	θ^a (')	Net Counts (0.35–8 keV)	$\log(pns)$ (0.35–8 keV)	$f_{0.35-8\text{ keV}}^b$ (10^{-15} erg s $^{-1}$ cm $^{-2}$)
(1)	(2)	(3)	(4)	(5)	(6)	(7)	(8)	(9)
7	121535.34+361752.0	183.8972800	36.297805	0.19	2.1	11.1 $^{+4.6}_{-3.4}$	−9.1	1.0
8	121529.43+361545.4	183.8726600	36.262624	0.24	3.0	16.1 $^{+5.2}_{-4.1}$	<−10	2.3
9	121528.30+361644.1	183.8679200	36.278920	0.26	3.3	33.1 $^{+7.1}_{-6.0}$	<−10	3.1
10	121536.06+361847.3	183.9002900	36.313160	0.18	2.0	10.3 $^{+4.4}_{-3.3}$	−9.3	0.9

Notes.

^a θ is the off-axis angle from the *Chandra* ACIS aim point. Sources marked with a * are “marginally detected” sources and are not included in subsequent analysis (see the text for further details).

^b Unabsorbed X-ray flux, assuming the power law with $\Gamma = 1.9$ absorbed by the appropriate Galactic column given in Table 1.

(This table is available in its entirety in machine-readable and Virtual Observatory (VO) forms.)

Table 6
Limiting Fluxes and Luminosities of Merged Observations

Galaxy	Energy band (keV)	70%		90%		95%		Minimum ^a	
		f_x^b	L_x^b	f_x	L_x	f_x	L_x	f_x	L_x
(1)	(2)	(3)	(4)	(5)	(6)	(7)	(8)	(9)	(10)
NGC 55	0.35–8	3.1	1.6	4.7	2.5	5.4	2.8	0.7	0.4
	0.5–2	0.8	0.4	0.6	0.3	2.2	1.2	0.2	0.1
	2–8	1.2	1.0	2.8	1.5	3.5	1.9	0.4	0.2
NGC 2403	0.35–8	1.3	1.7	2.5	3.2	3.9	5.0	0.4	0.5
	0.5–2	0.5	0.7	0.7	0.9	1.3	1.7	0.1	0.1
	2–8	0.8	1.1	1.4	1.9	2.1	2.8	0.3	0.4
NGC 4214	0.35–8	1.7	1.7	3.4	3.4	3.8	3.8	0.5	0.5
	0.5–2	0.3	0.3	1.1	1.1	1.2	1.2	0.1	0.1
	2–8	1.0	1.0	2.0	2.0	2.7	2.7	0.3	0.3

Notes.

^a The flux and luminosity of the faintest source meeting our *pns* threshold.

^b The units of flux are 10^{-15} erg s $^{-1}$ cm $^{-2}$ and the units of luminosity are 10^{36} erg s $^{-1}$.

and a “hard” color,

$$\text{HR2} = \frac{H - M}{H + M + S}. \quad (2)$$

We use the Bayesian Estimation of Hardness Ratios⁸ (BEHR; Park et al. 2006) to determine the HRs for each X-ray source in NGC 55, NGC 2403, and NGC 4214. For faint sources, the net counts in a band can be negative due to fluctuations in the source and background estimates, resulting in unphysical HRs when calculated using a traditional, non-Bayesian approach. The BEHR code accounts for the fact that source and background counts are non-negative, ensuring that all HRs are physically meaningful. In the high-count regime, the results of the Bayesian approach become equivalent to traditionally computed HRs.

While the BEHR code accounts for the fact that source and background counts are non-negative, it can only compute a HR for two input bands (e.g., only using H and S) and does not directly handle the three-band forms such as those defined above. We therefore use the BEHR code to construct 50,000 probability distributions for the S , M , and H counts. Using these distributions, we compute 50,000 values for HR1 and HR2 for each source. The HR value is defined as the mean of

the distribution, and the credible interval is evaluated based on the 68.2% equal-tail estimates (i.e., 0.682/2 of the samples have values below the lower limit, and 0.682/2 of the samples have values above the upper limit). We note that the median HR values (with a credible interval defined by the 16% and 84% values) did not differ significantly from the mean values reported.

For each source, the inputs to BEHR are source counts, background counts, the AE “backscale” parameter (which accounts for the ratio of the source and background extraction areas and efficiencies), and a factor converting from counts to photon flux (i.e., the exposure time multiplied by the mean ARF over the extraction region). We additionally set the “softeff” and “hardeff” parameters equal to the exposure time multiplied by the mean ARF values computed by AE for each observation in which the source was observed. The “eff” parameters take into account variations in effective area and exposure times between different observations and different energy bands, so that all HR calculations are normalized to the same instrument (e.g., one could correct for the differences in low-energy response of an ACIS-S detection when comparing to an ACIS-I detection). This is especially important considering the differences in ACIS filter contamination between the observations utilized in this work. For each energy band, we set

⁸ <http://hea-www.harvard.edu/AstroStat/BEHR/>

Table 7
Hardness Ratio Source Classification Scheme

Classification (1)	Definition (2)	# Sources ^a (3)
X-ray binary or AGN (“XRB/AGN”)	$-0.4 < \text{HR2} < 0.4, -0.4 < \text{HR1} < 0.4$	298
Absorbed source (“ABS”)	$\text{HR1} > 0.4$	69
Supernova remnant (“SNR”)	$\text{HR2} < 0.1, \text{HR1} < -0.4$	53
Indeterminate hard source (“HARD”)	$\text{HR2} > 0.4, -0.4 < \text{HR1} < 0.4$	19
Indeterminate soft source (“SOFT”)	$\text{HR2} < -0.4, -0.4 < \text{HR1} < 0.4$	18
Indeterminate source (“INDET”)	$\text{HR2} > 0.1, \text{HR1} < -0.4$	3

Notes.

^a The total number of sources in NGC 55, NGC 2403, and NGC 4214 with hardness ratios placing them in each category.

the BEHR “burnin” parameter to 50,000 and the “total draws” parameter to 100,000.

To aid in the interpretation of our HR calculations, we use a version of the X-ray color–color classification used in Kilgard et al. (2005) and Prestwich et al. (2003), modified here to account for our different definition of the HRs. The HR classes are described in Table 7. Column (1) lists the X-ray source classification category. Column (2) provides the definition of the classification category in terms of HR1 and HR2. Column (3) lists the number of sources falling within each classification. Six categories of X-ray sources are defined: “XRB/AGN”-like (which contains both XRBs and background AGN, given their similar HRs), “SNR”-like (which likely also contains foreground stars and SSSs), “ABS” for heavily absorbed sources, indeterminate “HARD” and “SOFT” sources, and “INDET” for sources with an indeterminate spectral shape. We note that these classifications are uncertain—for example, a heavily obscured SNR could exhibit X-ray colors consistent with being an “XRB/AGN”-like source. However, for low-count sources, HRs are the only method for constraining the underlying spectral shape. Additional information (e.g., variability, optical counterpart, etc.) is required to refine each source’s classification.

The HRs and corresponding source classifications for each galaxy are given in Table 8. Columns (1)–(4) provide the unique source number, HR1, HR2, and the classification, respectively, of the sources in NGC 55. Columns (5)–(8) provide the same information for sources in NGC 2403, and Columns (9)–(12) provide the corresponding information for sources in NGC 4214. Figure 2 shows the HR values for all sources with more than 20 net counts in the 0.35–8 keV band for all five CLVS galaxies, and hints at some differences in the X-ray source populations of the five CLVS galaxies. For example, NGC 404 (cyan) shows significantly fewer sources in the “SNR”-like category than the disk galaxies. This is not surprising, as one would not expect to find many SNRs in the older stellar populations and earlier morphology of NGC 404. The three “SNR”-like sources in NGC 404 are likely to be foreground stars. The top and right panels of Figure 2 show the cumulative fraction of sources at each HR for all five galaxies.

To compare the X-ray source populations of the five CLVS galaxies in a quantitative manner, we calculate the fraction of each HR class found for each galaxy and for the total CLVS sample (Table 9). Column (1) lists each galaxy, and Columns (2)–(6) provide the percentage (%) of X-ray sources in that galaxy falling within each classification as determined solely by their HRs. We find that most of the X-ray sources fall within

the “XRB/AGN” category ($\sim 58\%$ – 67%), with an additional $\sim 12\%$ – 20% of sources showing evidence for additional absorption beyond the Galactic column. These two categories make up approximately three quarters of all the X-ray point sources and are likely to contain the majority of XRBs associated with their host galaxies with some contamination from background AGN (whose X-ray spectra are similar to those of many XRBs).

The softer HR categories (i.e., “SNR” and “SOFT”) likely contain contamination by foreground stars. This is especially true for the $\sim 4\%$ X-ray sources in NGC 404 designated as “SNR”-like by their HRs. The fraction of “SNR”-type sources in NGC 404 is below the sample average by $\sim 3\sigma$, as would be expected when comparing an S0-type galaxy with very little recent star formation to the later-type spirals and irregulars. “SOFT” sources are observed in comparable fractions to “SNR”-like sources, and may consist of very soft XRBs, background sources with unusual absorption properties, or foreground objects. A small fraction of X-ray sources, $< 8\%$, are classified as “HARD.” These sources are likely background AGN that have experienced a high degree of absorption.

5.2. X-ray Spectral Analysis

For sufficiently bright sources, the X-ray spectrum can constrain the physical origin of the X-ray emission. Both XRBs and AGN are typically described by power laws, with photon indices ranging from $\Gamma \sim 1$ – 2 . If the source is a likely XRB, the photon index can sometimes be used to constrain the nature of the compact object: NS primaries typically exhibit harder X-ray emission, with $\Gamma < 1.5$, while BHs produce $\Gamma \sim 2$ – 2.5 (or softer) due to the lack of a solid surface (McClintock & Remillard 2006). Foreground stars and SNRs exhibit significantly softer X-ray emission with emission lines indicative of a thermal plasma.

Spectra were extracted by AE using the CIAO tool `dmextract`, and response files were created using `mkacisrmf` and `mkarf`. Due to the low number of counts found for the majority of sources, the traditional approach of binning the spectrum and using the χ^2 statistic would result in significant biases in our spectral models (especially at high energies). Instead, we utilize the unbinned spectra and the Cash statistic (see e.g., Cash 1979; Nousek & Shue 1989; Humphrey et al. 2009; Arnaud et al. 2011).

We define the C-statistic as our “fit statistic” (i.e., to be minimized during the fit) and use the Pearson χ^2 as our “test statistic” for the same fit. Additionally, we use the goodness

Table 8
Hardness Ratios of X-ray Sources

NGC 55				NGC 2403				NGC 4214			
No.	HR1	HR2	ID	No.	HR1	HR2	ID	No.	HR1	HR2	ID
(1)	(2)	(3)	(4)	(5)	(6)	(7)	(8)	(9)	(10)	(11)	(12)
1	0.22 ± 0.37	-0.38 ± 0.29	XRB	1	0.21 ± 0.07	0.41 ± 0.12	HARD	1	-0.59 ± 0.20	0.16 ± 0.17	SNR
2	0.45 ± 0.22	-0.49 ± 0.22	ABS	2	-0.13 ± 0.03	-0.16 ± 0.02	XRB	2	0.31 ± 0.12	-0.17 ± 0.14	XRB
3	0.30 ± 0.08	-0.22 ± 0.09	XRB	3	0.32 ± 0.10	-0.34 ± 0.09	XRB	3	0.21 ± 0.25	0.18 ± 0.39	XRB
4	0.38 ± 0.11	0.13 ± 0.20	XRB	4	0.36 ± 0.12	-0.23 ± 0.14	XRB	4	0.06 ± 0.14	-0.08 ± 0.14	XRB
5	0.47 ± 0.13	-0.35 ± 0.15	ABS	5	0.16 ± 0.24	0.20 ± 0.37	XRB	5	-0.44 ± 0.17	-0.19 ± 0.10	SNR
6	0.54 ± 0.28	-0.45 ± 0.38	ABS	6	-0.43 ± 0.20	-0.01 ± 0.16	SNR	6	0.24 ± 0.19	0.07 ± 0.26	XRB
7	0.25 ± 0.07	-0.23 ± 0.08	XRB	7	0.50 ± 0.09	-0.09 ± 0.16	ABS	7	0.31 ± 0.32	-0.30 ± 0.35	XRB
8	0.41 ± 0.05	-0.22 ± 0.07	ABS	8	0.33 ± 0.13	-0.05 ± 0.18	XRB	8	-0.17 ± 0.21	-0.23 ± 0.15	XRB
9	-0.12 ± 0.23	-0.30 ± 0.15	XRB	9	0.13 ± 0.08	-0.16 ± 0.08	XRB	9	0.44 ± 0.12	-0.15 ± 0.18	ABS
10	-0.22 ± 0.48	-0.00 ± 0.34	XRB	10	0.19 ± 0.12	-0.13 ± 0.12	XRB	10	-0.07 ± 0.15	0.67 ± 0.22	HARD

(This table is available in its entirety in machine-readable and Virtual Observatory (VO) forms.)

Table 9
Percentage (%) of Preliminary Classifications Based on Hardness Ratio Analysis

Galaxy (1)	XRB (2)	HARD (3)	SOFT (4)	SNR (5)	ABS (6)
NGC 55	58.4 ± 4.7	5.8 ± 0.5	6.4 ± 0.5	9.1 ± 0.7	20.1 ± 1.6
NGC 300	62.1 ± 6.4	8.4 ± 0.9	4.2 ± 0.4	8.4 ± 0.9	16.8 ± 1.7
NGC 404	60.8 ± 7.1	5.4 ± 0.6	9.5 ± 1.1	4.1 ± 0.5	20.2 ± 2.4
NGC 2403	65.8 ± 4.8	3.2 ± 0.2	3.2 ± 0.2	14.7 ± 1.1	12.6 ± 0.9
NGC 4214	67.2 ± 6.2	3.4 ± 0.3	3.4 ± 0.3	11.2 ± 1.0	14.7 ± 1.4
Total	62.9 ± 13.3	5.2 ± 1.1	5.3 ± 1.1	9.5 ± 2.0	16.9 ± 3.6

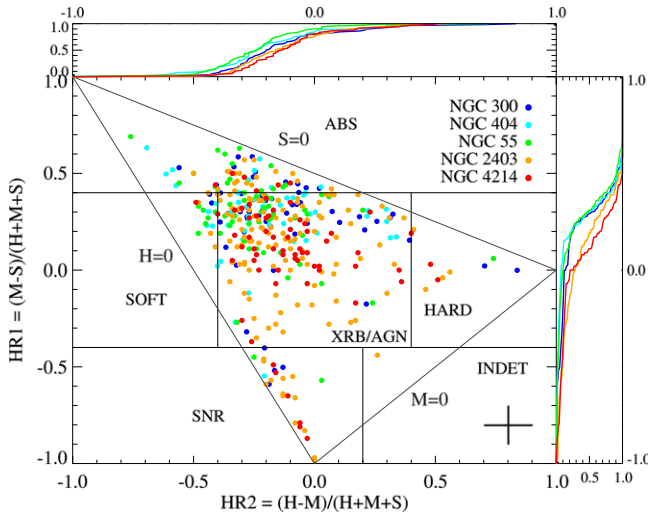


Figure 2. X-ray color-color diagram of all X-ray sources with more than 20 counts detected in the five CLVS galaxies. The thick cross in the lower-right corner shows the typical size of the errors. The diagram has been broken into preliminary source identification regions. The regions are labeled as: “ABS” for absorbed sources, “XRB/AGN” for X-ray binaries and AGN, “SNR” for supernova remnants, “SOFT” for indeterminate soft sources, “HARD” for indeterminate hard sources, and “INDET” for sources with an indeterminate spectral shape. The gray lines indicate the zero-count limits in the hard (“H”), medium (“M”), and soft (“S”) bands. The top and right panels show the cumulative fraction of sources at each HR for each of the five galaxies.

command (Arnaud 1996) to perform 5000 Monte Carlo simulations of each spectrum to evaluate the quality of the fit; if the observed spectrum was described well by that model, the “goodness” should be $\sim 50\%$. In most of the high-count cases (e.g., those sources with >500 counts), spectra with a goodness in the range of $\sim 40\%$ – 60% correspond with a minimized C -statistic and a reduced χ^2 near unity. While it has been shown (Cash 1979; Nousek & Shue 1989; Humphrey et al. 2009; Arnaud et al. 2011) that the C -statistic is preferable over χ^2 for sources with only a few hundred counts or less, both the C -statistic and χ^2 approaches converge when the number of counts in a spectrum is large. We therefore do not expect the “test” Pearson χ^2 to be a reliable indicator of fit quality for low-count sources. However, the “test” χ^2 of the best-fit models for those sources with >500 counts is consistently near unity.

We performed spectral fits for all sources with >50 net counts. For sources with <500 counts, the general shape of the source spectrum can be measured; for brighter sources with $\gtrsim 500$ counts, further details of the X-ray spectrum (e.g., thermal emission features) begin to become apparent. The spectral fitting results for all 136 sources with >50 net counts are provided in Table 10, and the 19 sources with >500 counts

are discussed in more detail in the following subsection. We used XSPEC v12.8.1g to perform all spectral fitting, and all errors represent the 90% uncertainties. All reported fluxes and luminosities are unabsorbed, unless otherwise noted.

Column (1) lists the source number in each galaxy. Column (2) provides the number of net counts observed in the 0.35–8 keV energy band. Sources with >500 net counts, discussed in detail below, are indicated with an asterisk. Column (3) lists the name of the best-fit model. Column (4) provides the amount of additional absorption beyond the Galactic column required by the spectrum. If no additional absorption was required, this field was left blank. Column (5) lists the power law photon index of the spectrum, if appropriate. This field is left blank for sources that did not require a power law component. Column (6) lists the temperature, in keV, of the thermal component of the spectrum, if appropriate. This field is left blank for sources that did not require a thermal component. Column (7) lists the degrees of freedom in each fit. Column (8) provides the C -statistic of the fit. Column (9) provides the Pearson χ^2 value of the fit. Columns (10) and (11) provide the unabsorbed fluxes yielded by the best-fit model, in the 0.5–2 keV and 0.35–8 keV bands respectively. Column (12) provides the goodness of the fit as indicated by the goodness command; values near $\sim 40\%$ – 60% indicate the spectrum is well described by the model.

5.3. Detailed Models of Bright Sources

Out of the combined 460 X-ray sources detected in NGC 55, NGC 2403, and NGC 4214, only 19 have more than five hundred net counts. In this subsection, we summarize the best fit spectral models found for each of these bright sources. A handful of these sources were sufficiently bright ($\gtrsim 10,000$ counts) that photon pile-up presented a concern; for these cases, we use the XSPEC model `pileup` to account for photon pile-up (Davis 2001).⁹ The spectra and corresponding best-fit models are shown in Figures 3–5, where they have been binned for display purposes only.

5.3.1. NGC 55

Source 23 has a total of 2692 net counts. Although the spectrum was obviously dominated by thermal emission, a single-component `apex` model provided a poor fit. The addition of a second `apex` component and a power-law component were necessary to provide an acceptable fit. We find no evidence for additional absorption beyond the Galactic column. This source was observed using *XMM-Newton*

⁹ See also xc.harvard.edu/ciao/download/doc/pileup_abc.pdf.

Table 10
Best-fit Spectral Models for X-ray Sources with ≥ 50 Counts

Source	Net Counts (0.35–8 keV)	Best-fit ^a	$N_{\mathrm{H}}^{\mathrm{b}}$ ($10^{21} \mathrm{cm}^{-2}$)	Γ	kT (keV)	dof ^c	C^{d}	χ^2_{e}	$f_{\mathrm{X}}^{\mathrm{f}}$ (0.5–2 keV) ($10^{-15} \mathrm{erg s}^{-1} \mathrm{cm}^{-2}$)	$f_{\mathrm{X}}^{\mathrm{f}}$ (0.35–8 keV) ($10^{-15} \mathrm{erg s}^{-1} \mathrm{cm}^{-2}$)	“Goodness ^g ” (%)
No. (1)	(2)	Model (3)	(4)	(5)	(6)	(7)	(8)	(9)	(10)	(11)	(12)
NGC 55											
3	81	po	...	2.0 ± 0.5	...	522	254	883	7.51	14.53	47
7	103	po	...	2.1 ± 0.5	...	316	177	280	11.37	21.48	64
8	169	po	...	1.3 ± 0.3	...	521	355	739	13.03	49.16	56
11	79	po	<2.2	$2.3^{+0.8}_{-0.6}$...	316	176	309	8.07	13.47	45
15	54	diskbb	$0.9^{+0.4}_{-0.3}$	521	180	727	4.15	7.40	55
23*	2692	po+2apec	...	2.7 ± 0.2	$0.3 \pm 0.1; 1.0 \pm 0.1$	449	358	477	261.0	307.4	62
37	123	po+apec	...	2.9 ± 0.1	1.0 ± 0.1	314	327	331	13.05	16.60	65
44	205	po	...	1.3 ± 0.2	...	521	356	509	112.54	386.60	45
52	65	apec	3.4 ± 1.3	521	247	460	3.75	7.94	47
54	439	po+apec	$2.8^{+0.4}_{-0.2}$	1.4 ± 0.3	0.3 ± 0.1	450	410	442	52.48	138.98	40
59	70	po	1.4 ± 0.3	521	225	680	4.83	15.26	58
62*	1786	po+diskbb	$2.9^{+0.9}_{-0.4}$	1.5 ± 0.1	<0.2	302	338	305	170.60	524.66	50
63*	2987	po	...	0.9 ± 0.1	...	453	420	455	254.87	460.45	53
67	139	po	...	$1.1^{+0.3}_{-0.2}$...	522	278	544	9.83	22.63	48
79	127	po	$4.3^{+0.4}_{-0.3}$	1.4 ± 0.6	...	304	247	288	12.35	40.46	42
80	55	diskbb	4.1 ± 0.2	...	1.4 ± 0.6	305	245	304	11.23	30.63	50
83	67	po	...	1.2 ± 0.8	...	168	143	223	6.92	27.74	71
91	200	po+diskbb	$8.0^{+0.2}_{-0.1}$	$1.4^{+0.3}_{-0.4}$	<1.0	439	385	474	145.33	211.74	58
95	104	po	...	1.1 ± 0.3	...	521	291	567	5.86	26.71	64
110	178	diskbb	0.9 ± 0.2	521	316	390	14.60	28.25	58
111	119	po	<2.8	$2.1^{+0.6}_{-0.5}$...	315	230	320	12.32	22.88	47
119 * _i	11523	po +diskbb +apec	<0.8	1.71 ± 0.18	disk 0.63 ± 0.06 apec 1.23 ± 0.06	449	474	469	1920.0	2990.0	59
122*	1516	po	1.5 ± 0.6	1.5 ± 0.1	...	520	499	460	116.4	370.90	58
126	89	po	57.1 ± 4.6	<0.8	...	521	298	481	7.93	71.37	43
128	60	brems	1.3 ± 0.6	522	248	541	6.00	7.93	86
130	110	po+diskbb	$4.0^{+0.2}_{-0.7}$	1.1 ± 0.5	<0.3	179	124	179	116.6	122.9	45
135	247	po	3.2 ± 0.2	$3.2^{+0.7}_{-0.6}$...	315	243	351	74.20	88.16	54
137	85	po	4.2 ± 0.3	2.7 ± 0.7	...	520	245	981	17.85	25.11	54
145	120	po	$4.1^{+0.3}_{-0.2}$	$1.7^{+0.6}_{-0.5}$...	520	308	572	16.45	39.69	53
147	71	po	...	$1.7^{+0.7}_{-0.5}$...	239	164	272	7.10	12.37	72
151	95	po	...	$1.4^{+0.4}_{-0.3}$...	521	271	404	7.21	23.41	64
152	66	po	...	<0.9	...	305	202	336	2.98	27.48	67
NGC 2403											
2*	904	po+2apec	...	1.4 ± 0.2	$<0.3; 0.67^{+0.1}_{-0.9}$	520	515	541	13.88	34.76	37
3	55	po	...	1.7 ± 0.5	...	315	170	340	1.48	3.70	43
9	82	diskbb	$0.5^{+0.2}_{-0.1}$	373	201	301	2.16	4.53	65
11	275	po+diskbb	...	$1.1^{+0.6}_{-0.7}$	0.2 ± 0.1	314	305	303	15.63	35.55	61
12	90	diskbb	$27.3^{+1.8}_{-1.1}$...	0.6 ± 0.3	509	298	473	31.80	41.71	61
19	115	po	...	$2.6^{+0.5}_{-0.4}$...	442	238	417	5.11	7.33	52
20	364	po	...	2.1 ± 0.2	...	316	274	341	5.51	10.33	65
23	57	diskbb	$0.6^{+0.5}_{-0.2}$	316	217	466	2.94	3.83	60
26	51	po	...	1.2 ± 0.6	...	267	141	297	5.17	21.26	56
29	161	apec	$35.5^{+12.8}_{-9.5}$...	4.0 ± 1.9	352	322	468	45.86	90.33	71
30	73	po	...	2.1 ± 0.5	...	521	235	355	4.42	8.48	52
31	149	po	$7.4^{+1.1}_{-0.7}$	1.5 ± 0.7	...	520	324	437	5.73	77.98	43
33	101	po	...	$3.3^{+0.5}_{-0.4}$...	316	192	231	18.70	21.78	65
39	62	po	...	2.4 ± 0.4	...	316	148	379	2.20	3.55	60
41 * _i	10033	po+diskbb	2.4 ± 0.1	2.8 ± 0.8	1.3 ± 0.2	517	538	536	340.5	667.1	64
42 * _i	16601	po+diskbb	3.3 ± 0.7	3.0 ± 0.6	1.1 ± 0.3	518	437	576	864.4	1568	41

Table 10
(Continued)

Source	Net Counts (0.35–8 keV)	Best-fit ^a	N_{H} ^b (10^{21} cm^{-2})	Γ	kT (keV)	dof ^c	C^d	χ^2_{ν} ^e	f_{X}^f (0.5–2 keV) ($10^{-15} \text{ erg s}^{-1} \text{ cm}^{-2}$)	f_{X}^f (0.35–8 keV) ($10^{-15} \text{ erg s}^{-1} \text{ cm}^{-2}$)	“Goodness ^g ” (%)
No. (1)	(2)	Model (3)	(4)	(5)	(6)	(7)	(8)	(9)	(10)	(11)	(12)
43	53	po	<4.6	2.3 ± 1.0	...	246	159	249	16.99	28.15	40
45	74	po	$2.0^{+0.3}_{-0.2}$	$1.7^{+0.7}_{-0.5}$...	520	244	615	2.01	4.95	54
48	93	po	...	1.7 ± 0.3	...	521	227	628	2.36	5.90	46
51*	658	diskbb	0.9 ± 0.1	384	328	400	15.99	29.70	60
52	62	po	...	$1.9^{+0.6}_{-0.5}$...	521	225	380	10.12	21.36	55
53	110	po	$5.8^{+0.4}_{-0.3}$	$2.0^{+0.8}_{-0.6}$...	520	294	673	5.38	10.52	66
55	112	apec	3.1 ± 1.0	384	222	402	2.37	4.79	52
57	105	po	<1.9	$1.7^{+0.6}_{-0.4}$...	304	227	330	2.47	6.34	66
58	54	po	...	<0.6	...	307	165	268	0.87	14.87	79
62*	5433	po+2apec	...	2.7 ± 0.1	$1.0 \pm 0.1; 0.3 \pm 0.1$	312	296	394	542.20	629.35	40
64*	772	apec+apec	$0.2 \pm 0.1; 0.9 \pm 0.1$	136	140	137	22.92	23.92	44
72	53	diskbb	$0.5^{+0.4}_{-0.2}$	523	202	409	2.32	2.96	59
78*	541	po+apec	...	1.9 ± 0.2	1.0 ± 0.1	519	369	632	29.34	50.50	58
81	52	po	$6.1^{+0.6}_{-0.4}$	2.1 ± 0.8	...	520	197	638	2.94	5.49	53
84	58	po	...	1.1 ± 0.4	...	316	196	326	0.92	4.26	54
86	83	po+diskbb	...	<0.5	<0.3	508	307	672	1.51	21.04	63
92*	5375	po+diskbb	...	1.9 ± 0.9	$1.7^{+0.1}_{-0.2}$	519	525	540	103.84	332.57	55
94	62	po	$15.5^{+0.7}_{-0.4}$	$2.1^{+1.0}_{-0.6}$...	520	245	427	11.16	26.35	65
96	87	apec	$7.4^{+0.4}_{-0.3}$...	0.2 ± 0.1	109	84	169	160.70	160.70	67
97	119	po	...	3.4 ± 0.4	...	316	237	328	16.25	18.47	49
106	315	po	...	1.7 ± 0.2	...	521	301	698	20.04	48.80	56
109	81	po	...	1.3 ± 0.4	...	521	273	441	1.32	4.75	42
110	59	po	...	0.9 ± 0.5	...	521	469	472	2.52	14.39	51
113	56	diskbb	<0.2	282	71	261	2.01	2.01	48
114	85	po	...	1.4 ± 0.4	...	521	288	420	4.32	15.43	55
117	61	po	...	<0.7	...	521	253	594	0.63	6.80	58
118	54	po	...	4.1 ± 0.8	...	521	358	401	4.73	4.98	64
119	90	po	<4.4	$1.7^{+0.6}_{-0.5}$...	520	272	556	6.21	16.14	45
120	84	po	...	$1.2^{+0.5}_{-0.4}$...	521	474	493	7.77	29.99	44
122	134	diskbb	2.0 ± 0.5	521	333	610	6.51	24.13	52
124	60	po	$7.6^{+0.8}_{-0.5}$	$1.3^{+0.8}_{-0.7}$...	520	245	550	4.59	17.00	53
128	141	po	...	1.2 ± 0.2	...	384	289	393	2.00	8.28	52
130	203	po	...	1.4 ± 0.2	...	522	360	499	20.79	71.53	54
132	61	po	...	3.4 ± 0.5	...	316	115	487	0.95	1.08	67
133	109	apec	<0.17	316	235	199	1.45	8.89	53
135*	1258	apec+apec	0.9 ± 0.3	...	$6.1 \pm 1.4; 1.0 \pm 0.1$	313	335	313	22.37	49.81	55
136	125	po	...	$2.2^{+0.4}_{-0.3}$...	316	274	369	7.87	14.16	59
140	248	po	4.3 ± 0.2	1.7 ± 0.3	...	520	380	543	10.66	26.03	50
141	57	po	...	<0.4	...	520	250	522	0.29	7.00	40
142	55	po	...	$0.9^{+0.9}_{-0.6}$...	453	272	376	3.19	17.66	64
145	82	po	<4.9	1.9 ± 0.9	...	315	236	498	13.98	28.55	40
149	53	po	...	2.2 ± 0.7	...	316	232	802	8.84	15.58	57
151	78	po	...	$2.1^{+0.6}_{-0.5}$...	521	343	480	10.26	19.01	53
152	72	po	...	$1.5^{+0.6}_{-0.5}$...	453	247	389	6.06	18.23	60
155*	1318	po	3.1 ± 0.5	1.1 ± 0.2	...	448	504	451	21.26	99.55	50
157	270	po	1.9 ± 0.9	$2.3^{+0.5}_{-0.4}$...	520	333	451	30.93	51.26	57
162*	957	po	1.0 ± 0.4	2.0 ± 0.2	...	520	422	565	28.06	55.81	62
164	67	diskbb	$0.5^{+0.4}_{-0.1}$	308	178	306	2.00	2.38	48
165	170	po	...	2.0 ± 0.3	...	308	178	306	4.91	10.01	65
169	345	diskbb	<0.2	316	180	146	49.55	49.56	42
170*	599	po	3.3 ± 0.8	1.8 ± 0.2	...	520	445	512	18.83	42.30	41
171	69	po	22.9 ± 16.9	$1.9^{+1.4}_{-1.2}$...	311	221	303	8.60	18.63	37
173	67	po	...	1.9 ± 0.4	...	420	215	685	2.54	5.67	57
174	464	po	1.8 ± 0.8	$1.9^{+0.4}_{-0.3}$...	315	368	404	15.18	31.92	44

Table 10
(Continued)

Source	Net Counts (0.35–8 keV)	Best-fit ^a	N_{H} ^b	Γ	kT	dof ^c	C^d	χ^2_e	f_{x}^f (0.5–2 keV)	f_{x}^f (0.35–8 keV)	“Goodness ^g ”
No. (1)	keV (2)	Model (3)	(10^{21} cm^{-2}) (4)	... (5)	(keV) (6)	... (7)	(8)	... (9)	($10^{-15} \text{ erg s}^{-1} \text{ cm}^{-2}$) (10)	(11)	(%) (12)
179*	1352	po	6.0 ± 0.7	2.2 ± 0.2	...	453	493	466	82.36	145.95	58
182	104	po	...	$1.5^{+0.4}_{-0.2}$...	384	256	479	3.94	11.50	54
186	76	po	...	1.8 ± 0.3	...	453	185	542	1.33	3.06	60
187	119	diskbb	<0.1	42	48	47	1.66	1.66	58
188	96	po	...	2.2 ± 0.5	...	454	303	430	7.29	12.97	64
NGC 4214											
16*	1827	po	1.5 ± 0.4	1.8 ± 0.1	...	317	312	286	92.29	213.38	54
17	347	apec+apec	3.9 ± 0.9 ; $0.6^{+0.2}_{-0.4}$	519	362	471	23.99	47.92	58
22	198	po	$1.3^{+1.6}_{-0.6}$	$2.1^{+0.7}_{-0.5}$...	318	319	305	27.38	51.48	43
24	78	po	...	$3.1^{+0.8}_{-0.6}$...	453	421	419	12.19	14.94	59
27	58	po	...	$1.0^{+0.3}_{-0.2}$...	385	252	832	2.39	11.94	60
28	60	brems	<27.9	...	<1.3	476	202	437	13.34	14.03	75
30	52	po	...	2.5 ± 0.8	...	454	219	396	3.94	5.57	66
32	62	apec	6.3 ± 1.6	318	176	335	2.31	6.35	66
33	94	po	...	2.5 ± 0.5	...	522	296	469	11.81	17.84	65
35	72	po	...	1.9 ± 0.4	...	521	213	324	7.80	16.48	57
37	185	po	7.3 ± 0.3	$1.6^{+0.5}_{-0.4}$...	521	378	603	28.23	73.60	41
38	89	po	...	3.0 ± 0.5	...	521	233	426	11.15	14.07	50
42	380	po	3.1 ± 0.1	2.1 ± 0.3	...	315	330	323	31.66	58.11	58
52	70	apec	$2.2^{+1.6}_{-1.4}$	521	235	458	5.90	9.70	59
53	181	po	4.0 ± 0.2	2.2 ± 0.5	...	521	322	656	16.45	29.10	42
61	131	po	...	1.7 ± 0.3	...	454	202	425	23.69	64.69	55
62	432	po+apec	1.3 ± 0.1	1.5 ± 0.3	$0.3^{+0.4}_{-0.1}$	450	388	470	20.55	53.91	60
68	53	po	...	$1.8^{+0.5}_{-0.4}$...	386	173	311	1.98	4.75	67
72	85	po	...	2.0 ± 0.4	...	521	356	473	14.53	28.43	50
76	81	po	...	<6.8	...	316	165	338	1.14	1.15	68
77	390	po+diskbb	...	$1.7^{+0.2}_{-0.4}$	<0.3	451	355	447	53.82	121.68	41
78	96	po	$6.2^{+0.6}_{-0.4}$	4.6 ± 1.0	...	315	261	426	244.96	251.13	51
79	65	po	...	$3.3^{+0.8}_{-0.7}$...	521	364	459	8.60	10.09	64
82	74	po	$4.0^{+0.3}_{-0.2}$	$1.8^{+0.8}_{-0.6}$...	520	213	547	5.62	12.73	54
83	94	po	...	2.5 ± 0.5	...	316	228	254	14.86	22.37	67
93	92	po	$9.7^{+0.5}_{-0.4}$	$2.3^{+0.8}_{-0.6}$...	509	242	425	15.57	25.41	59
109	60	po	...	$1.6^{+0.6}_{-0.5}$...	306	187	341	6.10	16.11	62
110	82	po	...	$3.5^{+1.5}_{-0.9}$...	521	459	478	8.66	9.66	51
112	76	brems	<6.4	521	502	509	5.15	5.89	57

Notes.

^a The best-fit model: po refers to a power law; apec is the thermal emission model; diskbb is a disk blackbody; *brems* refers to bremsstrahlung emission. All models include a Galactic absorbing column.

^b Intrinsic source absorption, if beyond the Galactic column was required.

^c Degrees of freedom.

^d Cash statistic.

^e Pearson χ^2 .

^f Unabsorbed X-ray fluxes.

^g Results of the XSPEC “goodness” command, run using 5000 realizations.

^h Sources marked with an asterisk contain more than 500 net counts and are discussed further in the text.

ⁱ Model includes pile-up component.

(Stobbart et al. 2006a, their source 39), and a Galactic RS CVn origin was suggested to explain the X-ray emission. Our low value of the absorption column and consistent thermal plasma temperatures support this conclusion.

Source 62 has a total of 1786 net counts detected in the archival *Chandra* observations. A two-component model consisting of a power law and disk blackbody with

additional absorption beyond the Galactic column was necessary to produce an acceptable fit. These results are comparable to those found by (Stobbart et al. 2006a, their source 47) using *XMM-Newton*. The inferred 0.35–8.0 keV X-ray luminosity of source 62 ($\sim 2.8 \times 10^{38} \text{ erg s}^{-1}$) is near the Eddington luminosity of a $\sim 2 M_{\odot}$ compact object, consistent with an LMXB.

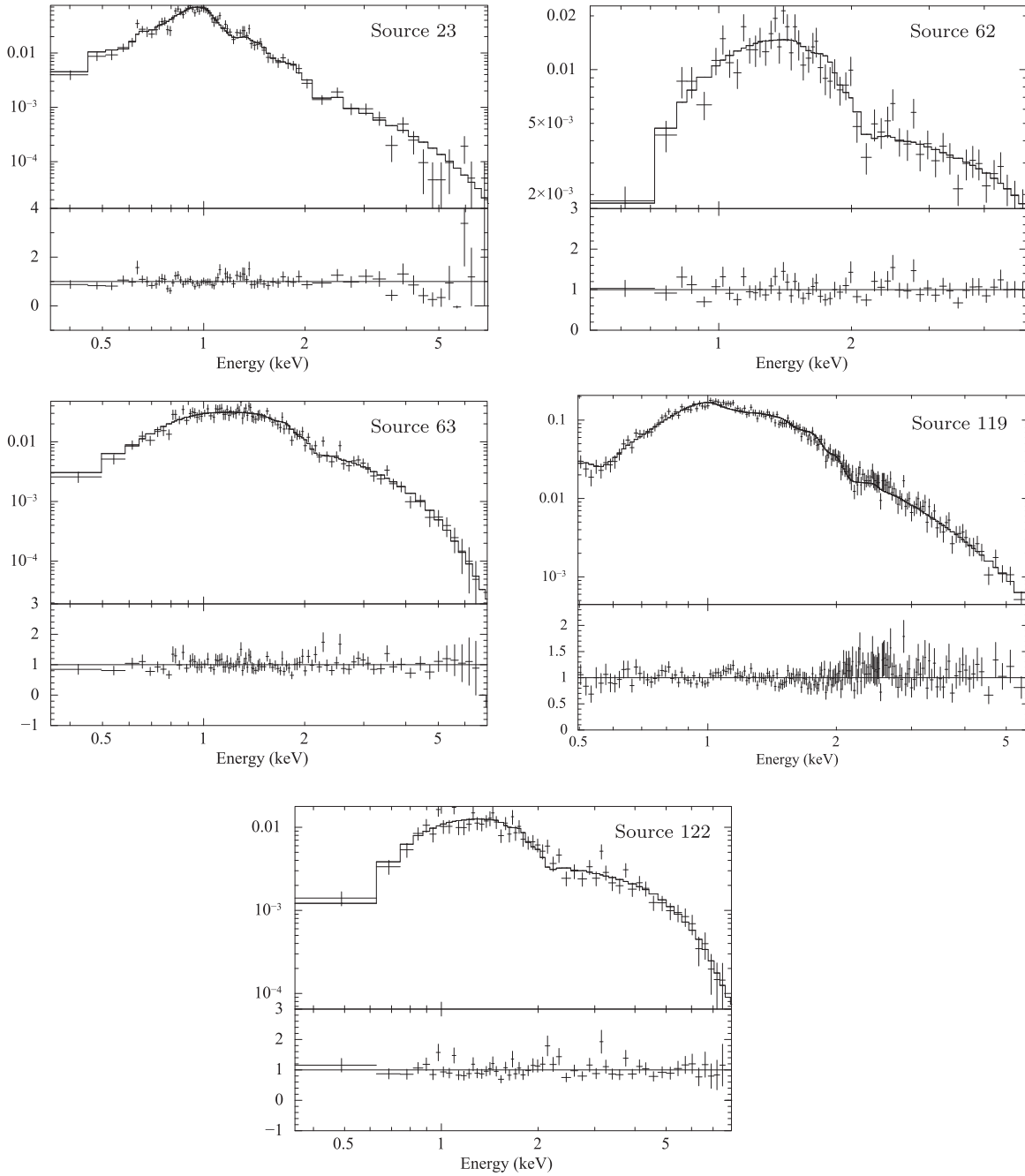


Figure 3. The spectra (with best fit models superimposed) and residuals for the NGC 55 sources with more than 500 net counts. Spectra are binned for display purposes only.

Source 63 contained 2987 counts. Although the *XMM-Newton* spectrum (Stobbart et al. 2006a, their source 43) was best fit by an absorbed power law ($\Gamma = 0.82 \pm 0.04$) and disk blackbody ($kT_{\text{in}} = 4.92^{+0.74}_{-0.78}$ keV) model, we did not require an additional disk blackbody to obtain an acceptable fit. Instead, our best fit model to the archival *Chandra* data was a single-component power-law with an index of 0.9 ± 0.1 , comparable to the power-law component measured from the *XMM-Newton* observations.

Source 119 is the NGC 55 ULX designated XMMU J001528.9-391319 Stobbart et al. (2004). It was detected in the archival *Chandra* observations with 11,523 net counts. Due to the large number of counts detected for this source, we

included pile-up in our spectral model. The estimated fraction of frames in the ACIS detector that have detected two or more pileup events is $\sim 5\%$ (see footnote above). The grade migration factor α was allowed to vary; we found a best-fit value of 0.28 ± 0.04 . Due to the large number of counts in the spectrum, our best fit model included three components: a power law, a thermal plasma, and a disk blackbody, all subject to absorption in excess of the Galactic column. The implied 0.35–8 keV luminosity for our best-fit model is 1.4×10^{39} erg s $^{-1}$. Taken at face value, this luminosity implies a BH mass of $\sim 12 M_{\odot}$, consistent with the Stobbart et al. (2004) result that this source is a dipping BH binary with a mass of $>11 M_{\odot}$ and

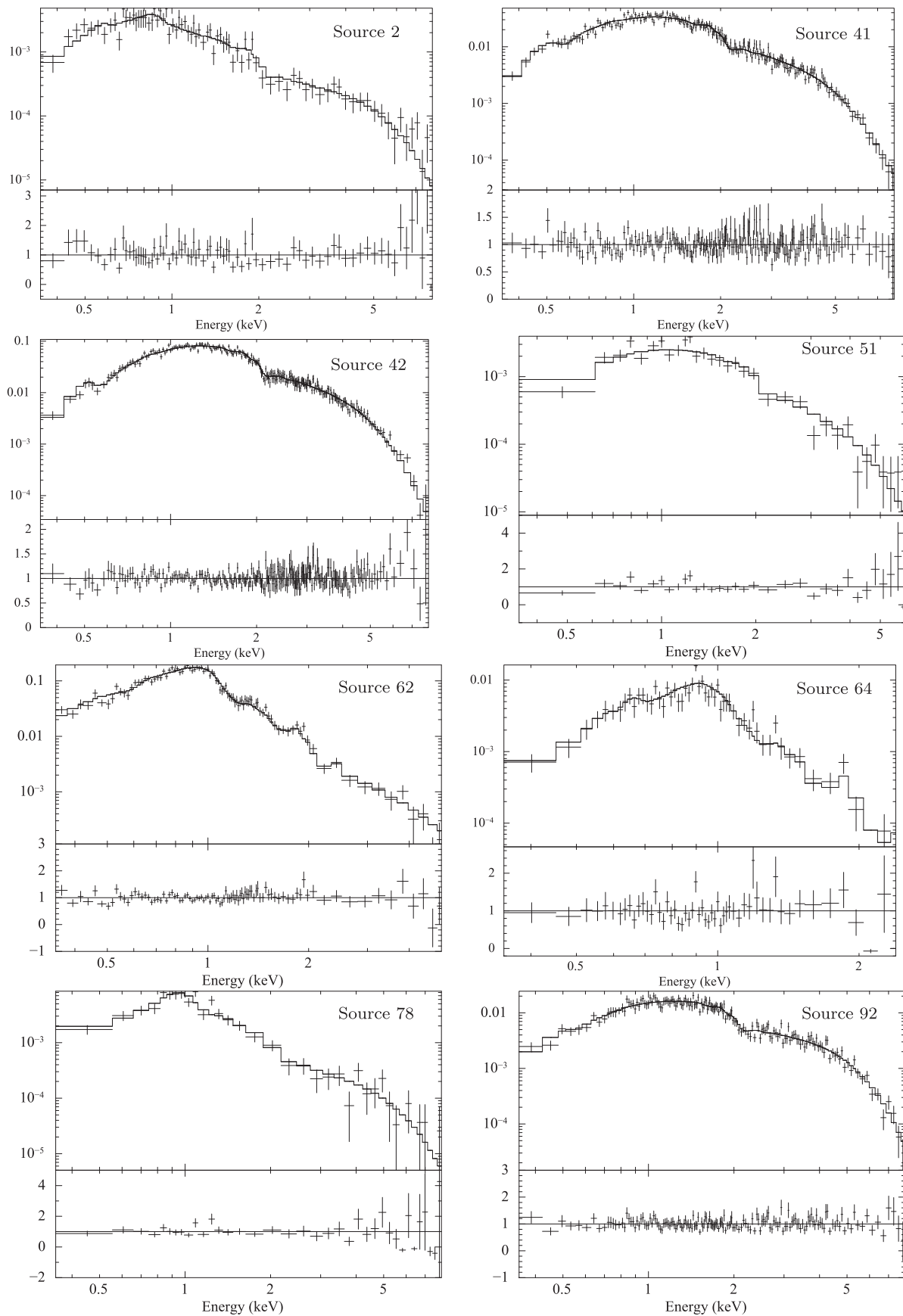


Figure 4. The spectra (with best fit models superimposed) and residuals for the NGC 2403 sources with more than 500 net counts. Spectra are binned for display purposes only.

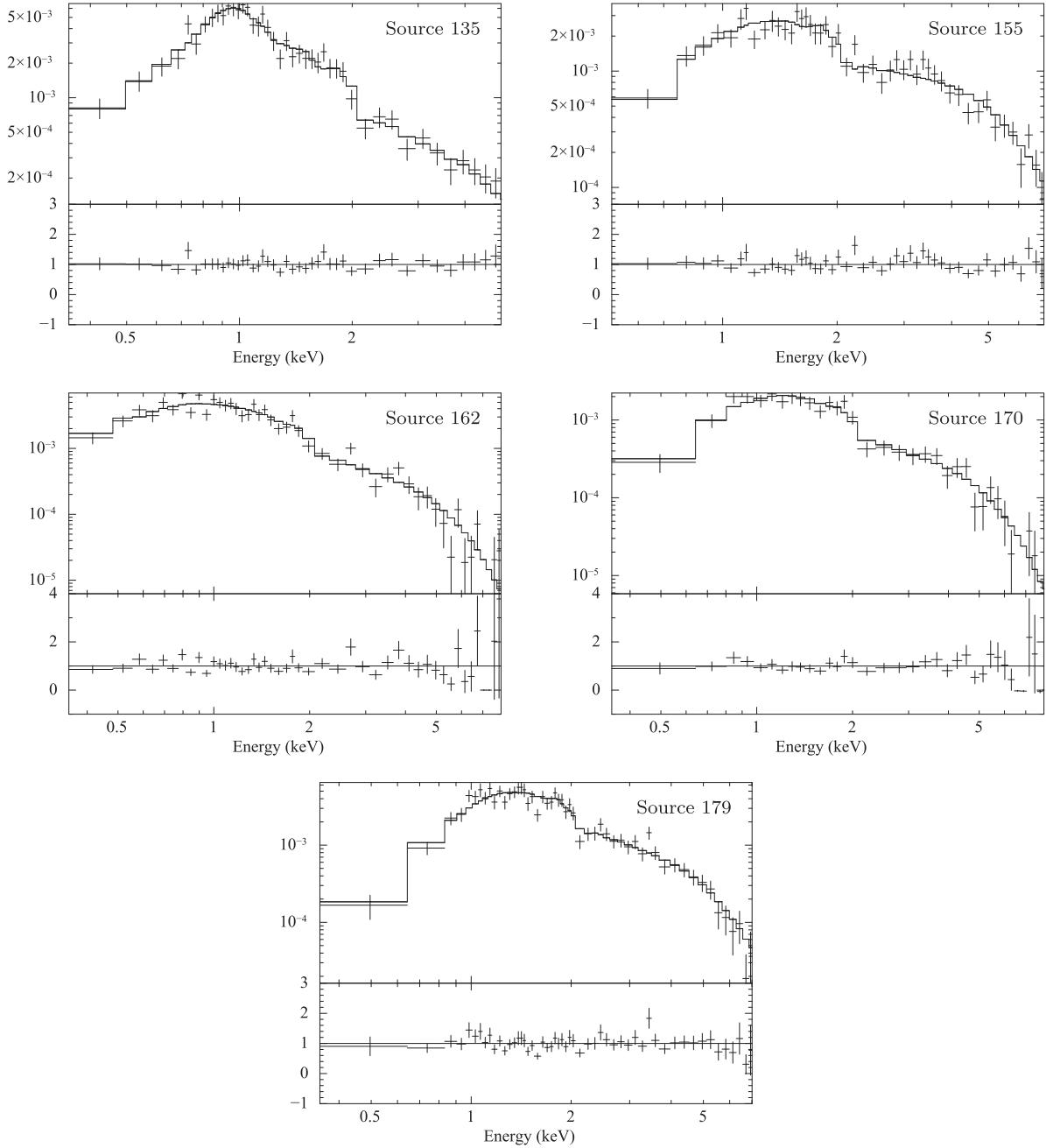


Figure 4. (Continued.)

whose luminosity varied from $8.9 \times 10^{38} \text{ erg s}^{-1}$ to $1.6 \times 10^{39} \text{ erg s}^{-1}$ in the 0.5–10 keV energy band. The thermal components account for $\sim 90\%$ of X-ray flux, somewhat different from the results of Stobbart et al. (2004), who observed nearly $\sim 100\%$ of the X-ray flux originating in the power law component at the beginning of the *XMM-Newton* observation and $<27\%$ of the flux from the power law component toward the end of their observation.

Source 122 has a total of 1516 net counts in the archival *Chandra* observations. We find the best fit model is an absorbed power law. The implied 0.35–8 keV luminosity of the source is $\sim 2 \times 10^{38} \text{ erg s}^{-1}$, consistent with a $\sim 1.4 M_{\odot}$ NS accreting at the Eddington limit.

5.3.2. NGC 2403

Source 2 has a total of 904 net counts in the 0.35–8 keV energy band. A three component model consisting of a power law with two thermal emission components was necessary to produce an acceptable fit. No absorption beyond the Galactic column is necessary to fit the spectrum. At the distance of NGC 2403, the best-fit model flux corresponds to a luminosity of $4.5 \times 10^{37} \text{ erg s}^{-1}$ in the 0.35–8 keV band.

Source 41 was designated source 20 in a previous analysis of Obs ID 2014 only (Schlegel & Pannuti 2003). The spectrum was found to be equally well-fit with bremsstrahlung emission with $kT \sim 3.5\text{--}4 \text{ keV}$ or a power law with $\Gamma \sim 1.9$. A total of 10,033 net counts were detected in the 0.35–8 keV energy band

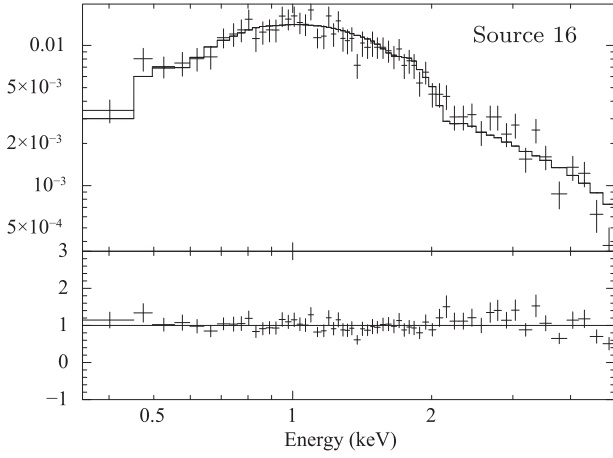


Figure 5. The spectrum (with best fit models superimposed) and residuals for source 16, the only NGC 4214 source with more than 500 net counts. Spectra are binned for display purposes only.

from all available *Chandra* observations. The spectrum was best fit by a power law plus a disk blackbody, and the results are similar to, but slightly softer than (Schlegel & Pannuti 2003). An additional absorption component was required in our model. Due to the large number of counts, we included pile-up in our model; the pile-up fraction was $\sim 3\%$. The 0.35–8.0 keV luminosity is $8.7 \times 10^{38} \text{ erg s}^{-1}$, making this a BH candidate.

Source 42 is a ULX, originally discovered by the *Einstein* observatory (Fabbiano & Trinchieri 1987), with a BH mass $M \sim 10\text{--}15 M_{\odot}$ (Isobe et al. 2009). Later observations with *ASCA* revealed a multi-color disk spectrum, with an innermost disk temperature of $kT_{\text{in}} \sim 1 \text{ keV}$ and an innermost disk radius of $R_{\text{in}} \sim 130 \text{ km}$ (Kotoku et al. 2000). Additional follow-up observations of this source with *Suzaku* and *Chandra* Obs ID 4628 are consistent with this model (Isobe et al. 2009), although the *Chandra* observation Obs ID 4630 is consistent with a power law model ($\Gamma \sim 2.7$), bremsstrahlung (with $kT \sim 1.8 \text{ keV}$), or a multicolor disk model ($kT_{\text{in}} \sim 0.6 \text{ keV}$ Schlegel & Pannuti 2003).

An acceptable fit to the 16,601 net counts in the 0.35–8 keV band for this source is reached using a power law plus a disk blackbody with a pileup fraction of $\sim 4\%$. The best-fit model yields a corresponding 0.35–8 keV luminosity of $\sim 2 \times 10^{39} \text{ erg s}^{-1}$ at the distance of NGC 2403. Taken at face value, this luminosity is consistent with a BH mass of $\sim 15 M_{\odot}$, consistent with the observations of Isobe et al. (2009).

Source 51 has 658 net counts in the 0.35–8 keV energy band. This source was previously classified as a transient source within the nuclear star cluster of NGC 2403 (Yukita et al. 2007). Previous work has found the X-ray spectrum of this source to be consistent with a disk blackbody model (Makishima et al. 1986, 2000). We also find the best fitting model to the 0.35–8 keV spectrum is a disk blackbody, and with a relatively low 0.35–8.0 keV luminosity of only $4 \times 10^{37} \text{ erg s}^{-1}$. We find no evidence for rapid variability, although the

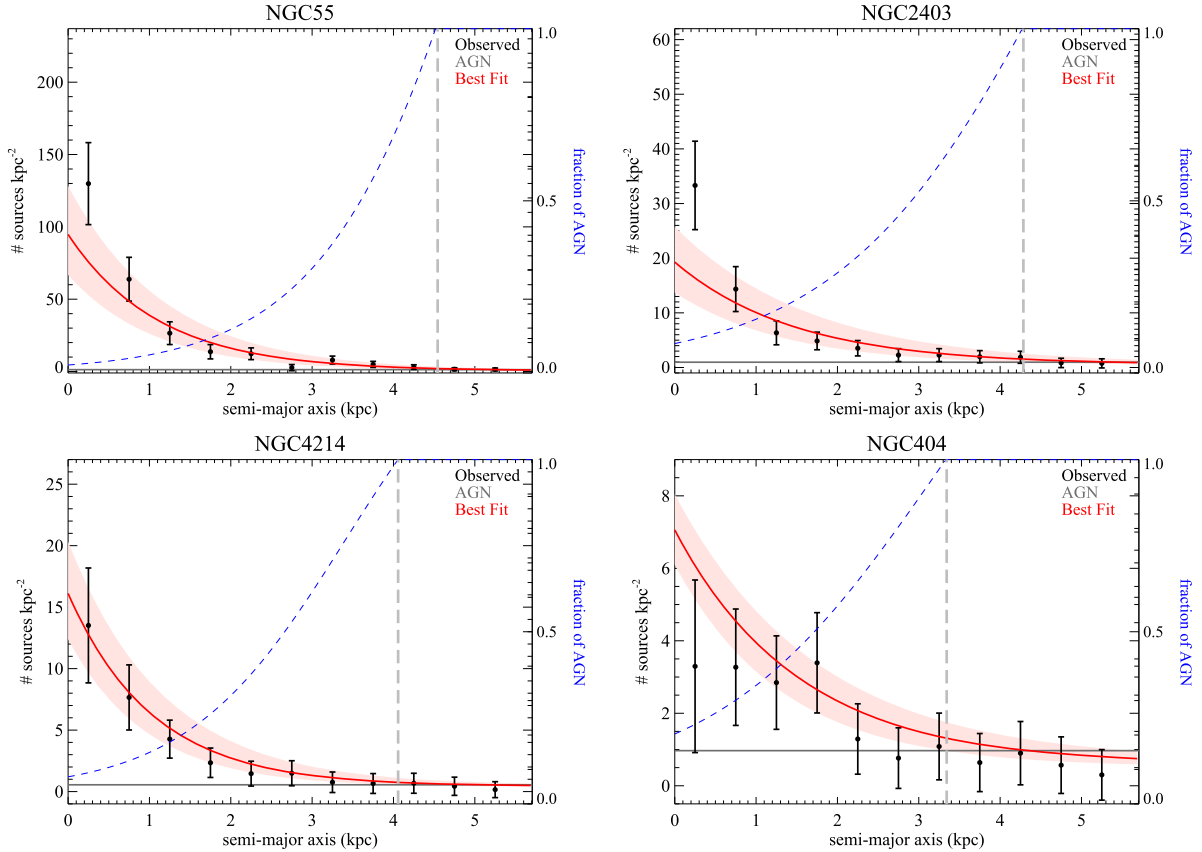


Figure 6. Radial source distributions. The total distributions (e.g., for all X-ray sources) are shown in black. The red line shows the best-fit exponential disk model (or a de Vaucouleurs model for NGC 404) to the data, and the 90% confidence region is shown in pink. The horizontal gray line indicates the expected number of AGN at each (de-projected) distance, and the vertical, dashed gray line shows the galactocentric distance at which the source density reaches the background level. The dashed blue line shows the predicted fraction of X-ray sources that are AGN as a function of distance. *Top left:* NGC 55; *top right:* NGC 2403; *bottom left:* NGC 4214; *bottom right:* NGC 404.

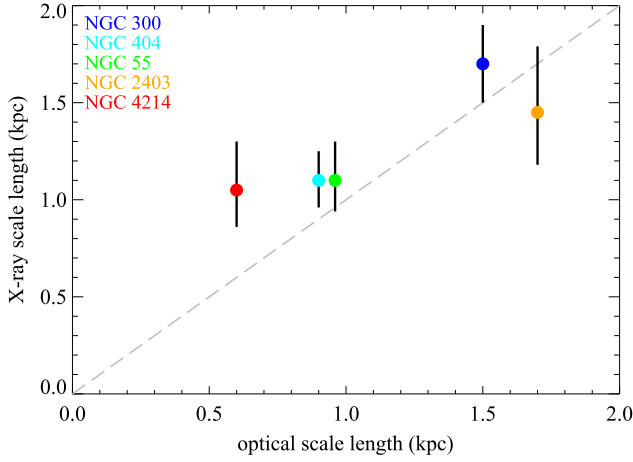


Figure 7. The X-ray scale lengths of each galaxy, derived from the radial source distribution for each galaxy, plotted against the optical scale lengths from the literature. The light gray dashed line shows a one-to-one correlation.

Table 11
AGN Contribution as a Function of De-projected Radius

Galaxy (1)	<10% (2)	25% (3)	50% (4)	75% (5)	100% ^a (6)
NGC 55	2.0 kpc	3.0 kpc	3.8 kpc	4.3 kpc	4.7 kpc
NGC 2403	0.8 kpc	2.1 kpc	3.2 kpc	3.9 kpc	4.5 kpc
NGC 4214	0.9 kpc	1.9 kpc	2.7 kpc	3.4 kpc	4.0 kpc
NGC 404	0.5 kpc	0.7 kpc	1.8 kpc	2.6 kpc	3.3 kpc

Note.

^a The radius at which 100% of X-ray sources are expected to be AGN is referred to in the text as r_{bkg} .

transient nature of the source is discussed in Yukita et al. (2007). The relatively soft X-ray emission and high X-ray luminosity in earlier observations ($\sim 7 \times 10^{38} \text{ erg s}^{-1}$) are suggestive of a BH with $M \sim 5 M_{\odot}$.

Source 62 required two thermal components and a power law to obtain a reasonable fit to the 5433 detected counts. We note that this X-ray source is coincident with a foreground star, with USNO-B1.0 apparent magnitudes of $m_B = 8.8$, $m_R = 8.1$, and $m_I = 7.9$. This source was also detected in the 2MASS catalog, with $J = 7.5$, $H = 7.2$, and $K = 7.1$. With a $R - I$ color of ~ 0.2 , the star is likely a mid-to-early F type. Assuming

an F-star absolute magnitude of ~ 3.5 implies a distance to the source of ~ 100 pc. We therefore estimate the 0.35–8 keV flux of Source 62 is $\sim 7.5 \times 10^{29} \text{ erg s}^{-1}$. Both the implied luminosity of Source 62 and the two-temperature thermal plasma fit to the spectrum are typical of other nearby F stars in the Milky Way (Micela et al. 1996; Prosser et al. 1996; Dahm et al. 2007).

Source 64 has a total of 772 net counts in the 0.35–8 keV energy band. The spectrum was best described with a two thermal emission components; the best fit model implies a 0.35–8.0 keV luminosity of $3 \times 10^{37} \text{ erg s}^{-1}$ at the distance of NGC 2403. Due to the soft, thermal spectrum, we also compute the corresponding luminosity of Source 64 assuming it is a foreground star. Assuming a distance of 4 kpc (an appropriate distance for a Milky Way object in the direction of NGC 2403, which is $\sim 30^\circ$ above the disk) yields a luminosity of $\sim 5 \times 10^{31} \text{ erg s}^{-1}$, typical of low mass stars.

Source 78 has 541 net counts, requires a power law plus a thermal emission component to provide an acceptable fit in the 0.35–8 keV energy band. This source was included in the USNO-B1.0 catalog with $m_R = 11.7$ and $m_I = 13.1$ and in the 2MASS catalog with $J = 13.4$, $H = 12.8$, and $K = 12.7$. The source has been identified as a K4III giant at a heliocentric distance of ~ 16 kpc (Pickles & Depagne 2010). At this distance, the corresponding X-ray luminosity is $1.5 \times 10^{33} \text{ erg s}^{-1}$ in the 0.35–8 keV band, and the X-ray-to-optical flux ratio $\log(f_X/f_V)$ of this source is -1.7 . A comparison to the Hunsch et al. (1998) catalog of X-ray emitting AFGKM giant stars shows that the implied X-ray luminosity of this source is 2–3 orders of magnitude higher than for other K-type giant stars, and it is not consistent with X-ray emission from main-sequence K- and F-type stars (Agüeros et al. 2009). It is therefore unlikely that this source is an isolated X-ray emitting star. The implied X-ray luminosity and X-ray-to-optical flux ratio are similar to Galactic bulge CVs (van den Berg et al. 2009); the observed rapid X-ray variability (see Section 5.5.2) is further consistent with a CV origin (Kuulkers et al. 2006). The properties of this source are also consistent with a NS accreting from the wind of a late-type giant (e.g., a symbiotic star, similar to GX 1 + 4; Masetti et al. 2006). However, our *HST* imaging does not cover this source, making it impossible for us to investigate whether its optical properties support the CV-origin scenario.

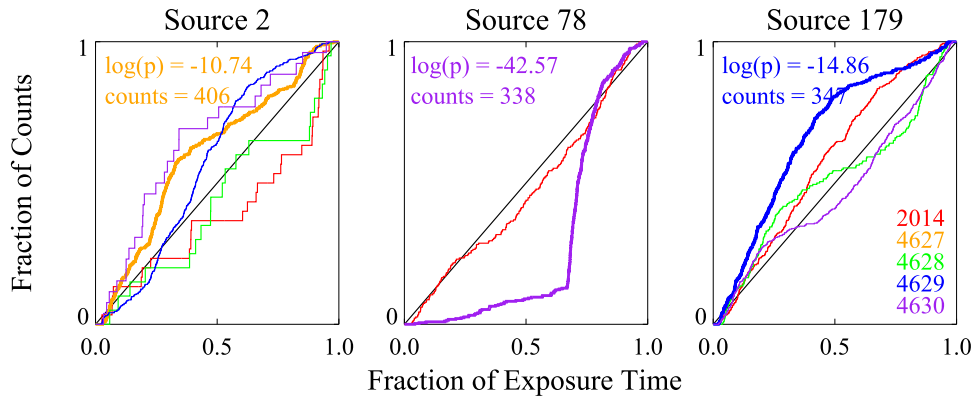


Figure 8. Cumulative photon arrival time distributions for X-ray sources in NGC 2403 showing evidence for rapid variability. The solid black line shows the expected distribution for a constant count rate. Colored histograms and text indicate the cumulative distribution observed and statistics for different observations. The (color encoded) *Chandra* Observation ID numbers are given in the rightmost panel. Each panel lists the (logarithmic) KS probability for no variability and the net 0.35–8 keV counts observed for each source.

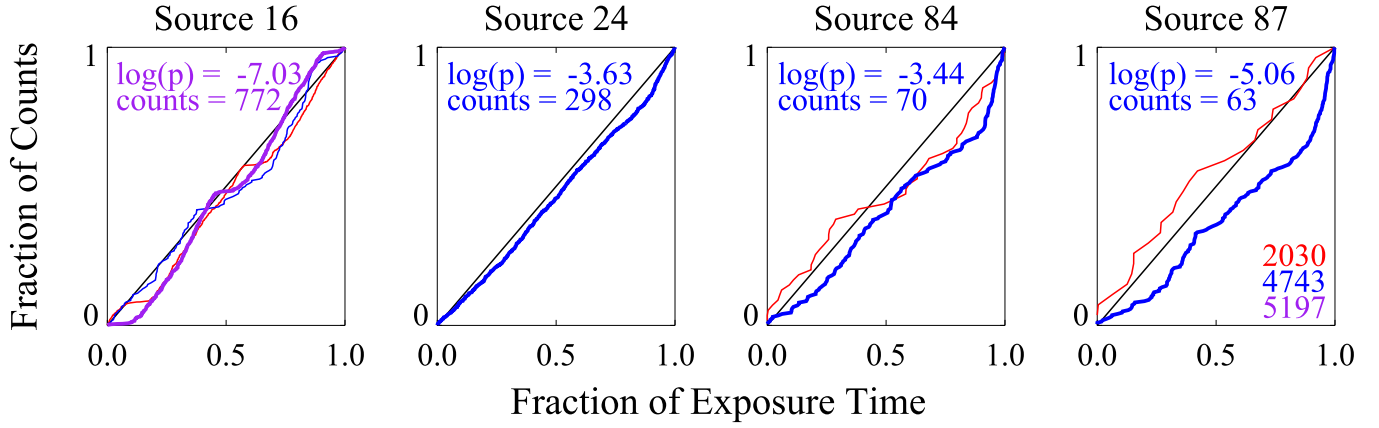


Figure 9. Cumulative photon arrival time distributions for X-ray sources in NGC 4214 showing evidence for rapid variability. The solid black line shows the expected distribution for a constant count rate. Colored histograms and text indicate the cumulative distribution observed and statistics for different observations. The (color encoded) *Chandra* Observation ID numbers are given in the rightmost panel. Each panel lists the (logarithmic) KS probability for no variability and the net 0.35–8 keV counts observed for each source in the observation with the lowest KS probability.

Table 12
Rapidly Variable X-ray Sources From *Chandra* Observations

Galaxy (1)	Source (2)	ξ^a (3)
NGC 2403	2	$10^{-10.74}$
NGC 2403	78	$10^{-42.57}$
NGC 2403	179	$10^{-14.86}$
NGC 4214	16	$10^{-7.03}$
NGC 4214	24	$10^{-3.63}$
NGC 4214	84	$10^{-3.44}$
NGC 4214	87	$10^{-5.06}$

Note.

^a The K–S probability of the source being constant within either *Chandra* observation.

Source 92 has a total of 5375 net counts. An acceptable fit to the spectrum requires a power law plus a disk blackbody as well as additional absorption. The fit yields a 0.35–8 keV luminosity at the distance of NGC 2403 of $4.3 \times 10^{38} \text{ erg s}^{-1}$. This source was designated source 1 in an earlier analysis (Schlegel & Pannuti 2003). The luminosity is near the

Eddington limit for a $\sim 3 M_{\odot}$ compact object, putting it into a very interesting mass regime near the transition between NSs and BHs. Our results therefore support the interpretation of this source as a LMXB.

Source 135 has been identified as SN 2004dj, which has an estimated progenitor mass of $14\text{--}15 M_{\odot}$ (Maíz-Apellániz et al. 2004; Wang et al. 2005; Vinkó et al. 2006). This source, whose X-ray spectrum has evolved significantly with time, has been analyzed in detail by Chakraborti et al. (2012). We perform a simpler analysis of the X-ray spectrum here for completeness. This source has a combined 1258 net counts and requires 2 thermal components to provide an acceptable fit. At the distance of NGC 2403, the best-fit model predicts a 0.35–8 keV luminosity of $6.5 \times 10^{37} \text{ erg s}^{-1}$. SN 2004dj is coincident with the compact cluster Sandage 96 (Yamaoka 2004), which is thought to host the progenitor star. For further discussion of the X-ray spectrum’s evolution, we refer the reader to Chakraborti et al. (2012).

Source 155 has 1318 net counts in the 0.35–8 keV energy band. The spectrum is well-fit by a simple and hard absorbed power law. At the distance of NGC 2403, the best-fit model implies a 0.35–8 keV luminosity of $1.3 \times 10^{38} \text{ erg s}^{-1}$.

Table 13
Long-term Variability of X-ray Sources From *Chandra* Observations

NGC 55			NGC 2403			NGC 4214		
No. (1)	η^a (2)	$\text{flux}_{\text{max}}/\text{flux}_{\text{min}}$ (3)	No. (4)	η^a (5)	$\text{flux}_{\text{max}}/\text{flux}_{\text{min}}$ (6)	No. (7)	η^a (8)	$\text{flux}_{\text{max}}/\text{flux}_{\text{min}}$ (9)
2	6.4	1.7	3	119	27.1	2	9.0	3.9
3	5.1	1.9	4	6.5	2.4	3	19.5	2.7
6	5.8	1.6	7	5.2	5.2	10	9.9	3.3
10	11.8	2.3	12	20.1	1.6	12	12.4	7.3
12	22.5	36.5	13	8.6	2.0	14	13.0	1.5
13	38.5	3.4	15	10.6	5.3	17	57.6	4.5
14	11.1	2.7	16	6.6	1.6	18	16.5	1.4
16	11.7	2.3	18	7.6	3.0	19	7.4	2.3
18	39.2	3.4	20	13.9	3.1	20	49.7	6.1
20	2255	142	21	20.8	9.2	21	47.8	18.5

Note.

^a η is the variability index defined by Türlmann et al. (2011) and is sensitive to long-term variability. Only sources with $\eta \geq 5$, indicative of a variability between the individual *Chandra* exposures, are shown.

(This table is available in its entirety in machine-readable and Virtual Observatory (VO) forms.)

Table 14
Long-term Variability Data for NGC 55 X-ray Sources

Source	0.35–8 keV flux (10^{-15} erg s $^{-1}$ cm $^{-2}$)				f_{\max}/f_{\min}	
	2001 Sep 11 ^a	2001 Nov 14 ^b	2001 Nov 15 ^c	2004 Jun 29 ^d	Detections	Upper Limits
(1)	(2)	(3)	(4)	(5)	(6)	(7)
3	2.45	24.33	<9.40	1.26	19.3	...
6	3.31	9.71	<6.37	5.15	2.9	...
7	3.17	51.74	29.14	<3.01	16.3	>17.2
8	0.83	48.11	51.81	<3.01	62.4	...
11	3.05	19.94	8.25	<3.01	6.5	>6.6
12	0.24	14.36	15.41	8.74	64.2	...
13	10.20	<6.84	13.13	<3.01	1.3	>4.4
14	2.26	<7.09	<6.28	6.02	2.7	...
15	2.74	14.98	5.72	3.98	5.5	...
16	3.27	<7.56	5.78	7.48	2.3	...

Notes.^a MJD 52176; *Chandra* Obs. ID 2255.^b MJD 52227; *XMM-Newton* Obs. ID 0028740201.^c MJD 52228; *XMM-Newton* Obs. ID 0028740101.^d MJD 53185; *Chandra* Obs. ID 4744.

(This table is available in its entirety in machine-readable and Virtual Observatory (VO) forms.)

Source 162 has a spectrum that is well-fit by a simple absorbed power law. This source contains 957 net counts. At the distance of NGC 2403, the best-fit model implies a 0.35–8 keV luminosity of 7.3×10^{37} erg s $^{-1}$.

Source 170 has 599 counts and a spectrum that is well-fit by a simple absorbed power-law. It's luminosity at the distance of NGC 2403 is about 5.5×10^{37} .

Source 179 has 1353 net counts. The 0.35–8 keV spectrum is also well-fit by an absorbed power law. At the distance of NGC 2403, the best-fit model implies a 0.35–8.0 keV luminosity of 1.9×10^{38} erg s $^{-1}$. The spectrum of this source was previously found to be consistent with either a power law with a photon index of ~ 2 (consistent with our best-fit model) or bremsstrahlung emission with a temperature of $kT \sim 4$ keV (Schlegel & Pannuti 2003, their source 28).

5.3.3. NGC 4214

Source 16 was previously designated CXOU J121538.2+361921 (Dewi 2006, their source 11) and has been identified as an XRB with a period of 3.62 hr and an X-ray luminosity of a few 10^{38} erg s $^{-1}$. It has been proposed that the system consists of a slightly evolved helium star with $M \sim 2\text{--}3 M_{\odot}$ and either a NS or low mass BH primary (Dewi 2006; Ghosh et al. 2006), although the favored interpretation is a NS-LMXB. This classification would make the system a direct progenitor of a double-NS binary. We detect 1,827 net counts in the 0.35–8 keV energy band for this source. The spectrum is well-fit by an absorbed power law, consistent with the analysis presented in Dewi (2006). The best fit model implies a 0.35–8 keV luminosity of 2×10^{38} erg s $^{-1}$ at the distance of NGC 4214. Our measurements are therefore consistent with others of this source, and we support the interpretation as a helium star-NS LMXB.

5.4. Radial Source Distributions

Following the radial source distribution analysis in Paper I, we assign an inclination-corrected, galactocentric distance to each X-ray source, assuming the galaxy center, inclination, and position angle for each host galaxy as given in Table 1. X-ray

Table 15
Long-term Variability Data for NGC 2403 X-ray Sources

Source	0.35–8 keV flux (10^{-15} erg s $^{-1}$ cm $^{-2}$)								f_{\max}/f_{\min}	
	2001 Apr 17 ^a	2003 Apr 30 ^b	2003 Sep 11 ^c	2004 Aug 9 ^d	2004 Aug 23 ^e	2004 Sep 12 ^f	2004 Oct 3 ^g	2004 Dec 22 ^h	Detections	Upper Limits
(1)	(2)	(3)	(4)	(5)	(6)	(7)	(8)	(9)	(10)	(11)
3	5.27	<35.09	<39.04	72.68	2.69	4.93	63.31	3.38	27.0	...
4	5.26	<34.49	<40.10	...	4.61	<5.34	2.22	...	2.4	...
7	1.09	54.21	51.21	...	0.64	24.60	1.71	0.33	164.3	...
12	62.95	<42.22	88.37	26.23	38.26	...	3.4	...
13	6.50	<22.39	<26.73	...	12.85	<4.84	<10.66	...	2.0	>2.7
15	1.55	<52.63	<62.05	...	6.30	<12.71	<8.22	...	4.1	...
16	8.37	<28.00	<26.33	...	13.39	8.95	<13.39	...	1.6	...
18	4.67	<34.24	<29.51	...	4.25	<5.29	<1.54	...	1.1	>3.0
20	6.17	<27.15	51.66	...	12.91	19.98	19.22	...	8.4	...
21	8.83	<29.23	<49.17	8.82	24.37	<4.87	2.65	13.30	9.2	...

Notes.^a MJD 52016; *Chandra* Obs. ID 2014.^b MJD 52759; *XMM-Newton* Obs. ID 0150651101.^c MJD 52893; *XMM-Newton* Obs. ID 0150651201.^d MJD 53226; *Chandra* Obs. ID 4627.^e MJD 53240; *Chandra* Obs. ID 4628.^f MJD 53260; *XMM-Newton* Obs. ID 0164560901.^g MJD 53281; *Chandra* Obs. ID 4629.^h MJD 53361; *Chandra* Obs. ID 4630.

(This table is available in its entirety in machine-readable and Virtual Observatory (VO) forms.)

Table 16
Long-term Variability Data for NGC 4214 X-ray Sources

Source	0.35–8 keV flux (10^{-15} erg s $^{-1}$ cm $^{-2}$)				f_{\max}/f_{\min}	
	2001 Oct 16 ^a	2001 Nov 22 ^b	2004 Apr 3 ^c	2004 Jul 30 ^d	Detections	Upper Limits
(1)	(2)	(3)	(4)	(5)	(6)	(7)
2	0.83	161.80	2.31	...	194.9	...
3	14.49	<36.74	...	5.30	2.7	...
10	5.13	<21.73	2.76	1.57	3.3	...
12	3.83	42.23	1.65	0.53	79.7	...
14	20.55	<60.51	...	31.65	1.5	...
17	213.01	<91.70	47.22	196.15	4.5	...
18	71.12	<46.42	50.87	60.43	1.4	...
19	4.44	<50.11	1.94	...	2.3	...
20	14.04	188.95	2.84	17.44	66.5	...
21	0.51	<30.64	9.44	...	18.9	...

Notes.

^a MJD 52198; *Chandra* Obs. ID 2030.

^b MJD 52235; *XMM-Newton* Obs. ID 0035940201.

^c MJD 53098; *Chandra* Obs. ID 4743.

^d MJD 53216; *Chandra* Obs. ID 5197.

(This table is available in its entirety in machine-readable and Virtual Observatory (VO) forms.)

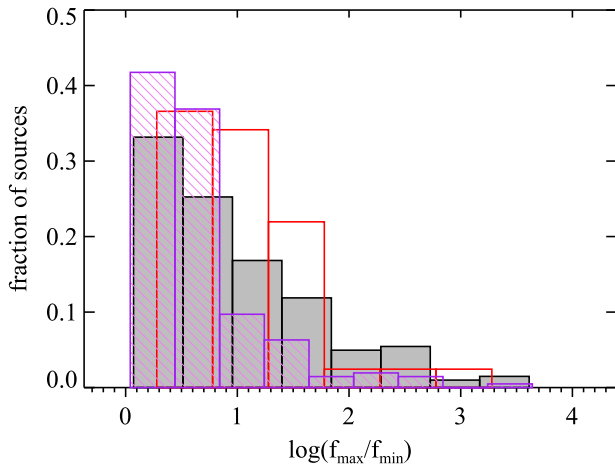


Figure 10. Histogram showing the maximum to minimum flux ratios from source detections (black) and upper-limits from source non-detections (red) using all available archival observations. The purple histogram shows the flux ratios using only the archival *Chandra* observations. The median flux ratio derived from source detections is ~ 5.8 ; the median flux ratio when utilizing upper-limits from source non-detections is 8.9. The *Chandra*-only flux ratio distribution has a median value of ~ 3.5 .

emitting foreground stars, found by visual inspection of both ground-based and *HST* imaging (see Section 6) were removed. X-ray sources are then divided into radial bins based on their inclination-corrected distances from the center of their host galaxy. We use our 0.35–8 keV sensitivity maps (discussed in Section 4.2) and the $\log N$ – $\log S$ distribution of Cappelluti et al. (2009) to estimate the expected contamination by background AGN in each bin. The 2–8 keV AGN flux provided by Cappelluti et al. (2009) is converted to a 0.35–8 keV flux assuming the standard model ($\Gamma = 1.9$ and N_H set to the Galactic value) with *WebPIMMS*.¹⁰ Since our observations are not sensitive to the full range of fluxes reported in the AGN $\log N$ – $\log S$ distribution (in general, our flux sensitivity

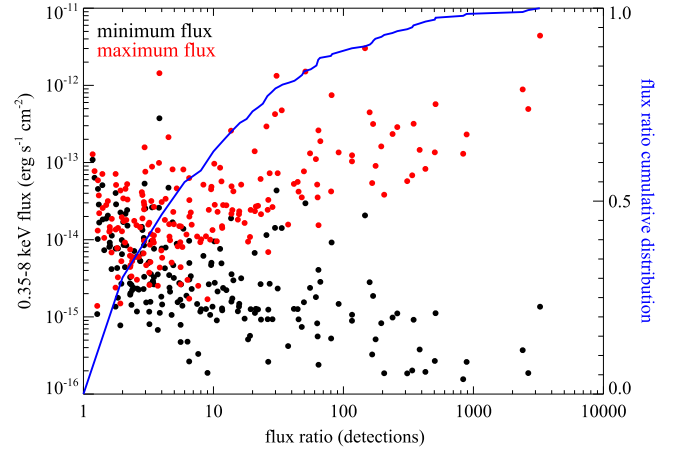


Figure 11. The minimum flux (black) and maximum flux (red) as a function of detected flux ratio. The blue line shows the cumulative distribution of the flux ratio determined from source detections.

decreases with increasing de-projected distance from the galaxy center), we only use the detected X-ray sources with fluxes above the minimum flux of our least sensitive radial bin.

Each radial source distribution was then fit to an exponential disk profile (or, in the case of NGC 404, a de Vaucouleurs profile) plus a constant term to represent the background, and the disk scale length (or, for NGC 404, the effective radius) was measured. The X-ray scale lengths obtained for NGC 55, NGC 2403, and NGC 4214 are $1.10^{+0.20}_{-0.19}$, $1.45^{+0.34}_{-0.27}$, and $1.05^{+0.25}_{-0.19}$ kpc, respectively. The X-ray effective radius found for NGC 404 is $1.10^{+0.17}_{-0.15}$ kpc. The radial source distributions and the best fit profiles are shown in Figure 6. The radial source distribution and fit for NGC 300 are described in Paper I. Figure 7 compares our X-ray results to the optical scale lengths found in the literature: 0.96 kpc for NGC 55 (Seth et al. 2005), 1.7 kpc for NGC 2403 (Barker et al. 2012), 0.6 kpc for NGC 4214 (Williams et al. 2011), and an effective radius of 0.9 kpc for NGC 404 (Baggett et al. 1998). The best-fit line through the data yields a slope of 0.68 ± 0.03 , and a Spearman-Rank test

¹⁰ <https://heasarc.gsfc.nasa.gov/cgi-bin/Tools/w3pimms/w3pimms.pl>.

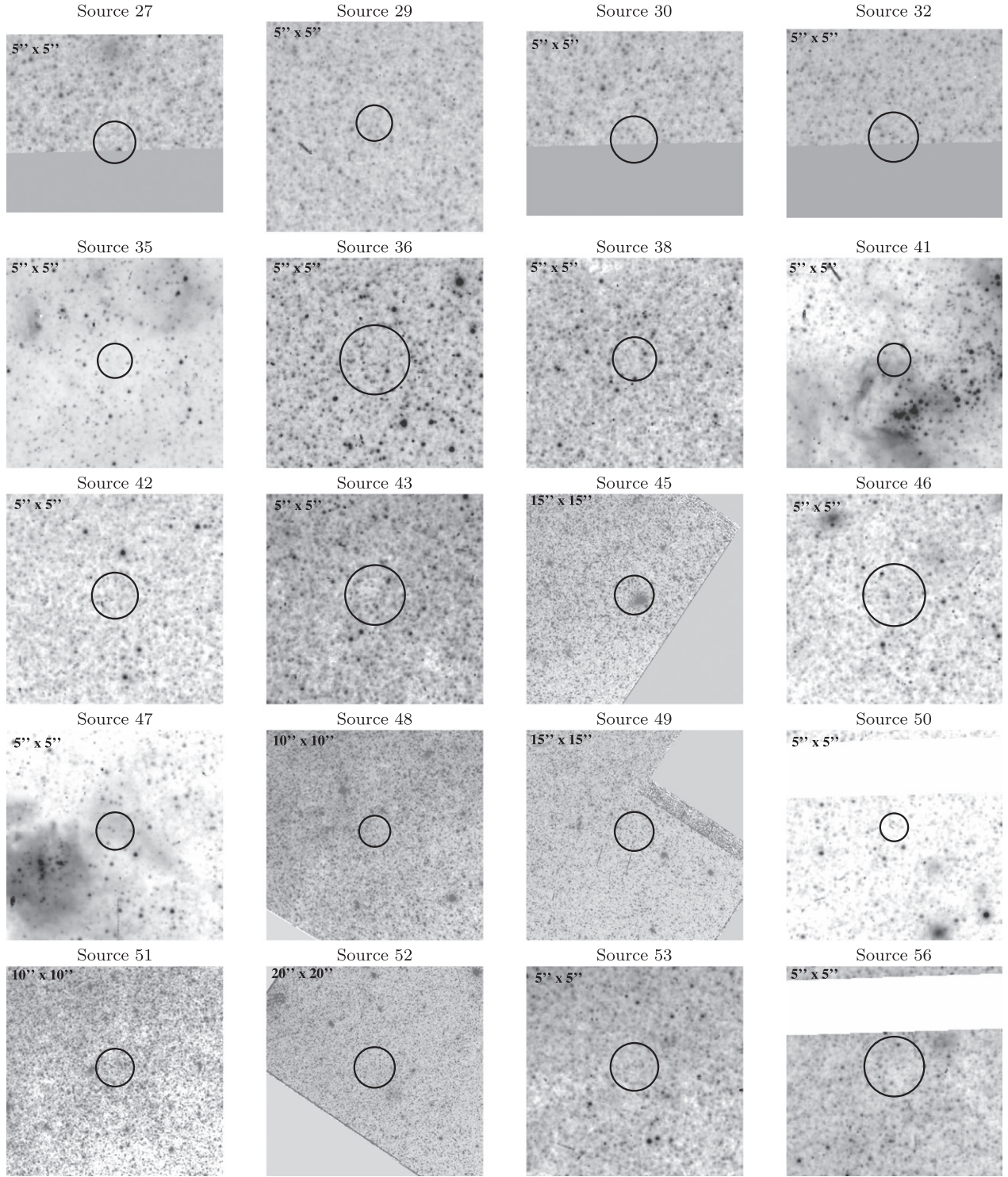
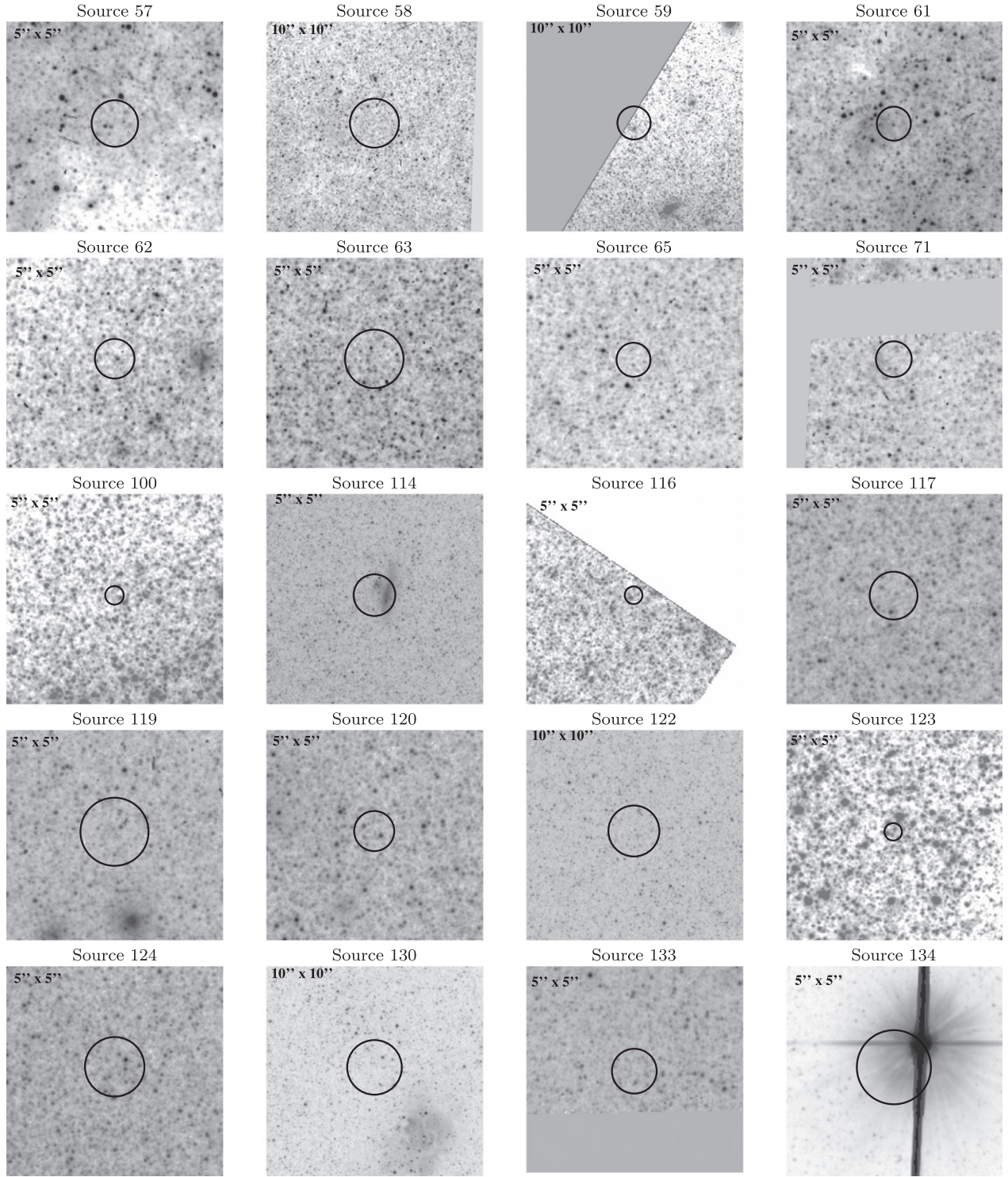


Figure 12. Optical *HST* images for X-ray sources detected in NGC 55. The box size ($5'' \times 5''$, $10'' \times 10''$, or $15'' \times 15''$) is given in the top-left corner of each image. The circle shows the *Chandra* 90% error circle, centered on the source position.

yields a $\sim 5\%$ probability of the X-ray and optical scale lengths being correlated. NGC 4214, the only dwarf irregular galaxy in our sample, shows the largest discrepancy between the X-ray and optical scale lengths, indicating the X-ray sources are more widely dispersed from the center than the optical light. This may be partially due to the ages of the underlying stellar populations: although the inner regions of NGC 4214 have recently (within the last ~ 100 Myr) experienced a vigorous

burst of star formation (Williams et al. 2011) resulting in a few HMXBs (which follow the light distribution), the majority of stars in NGC 4214 are old ($< 1\%$ of stars have ages $\lesssim 50$ Myr). LMXBs formed from these older stars would be expected to follow the mass distribution of the galaxy, which may have a larger scale length compared to the brightest stars. If we remove the NGC 4214 scale length from our sample, the slope of the best-fit line through the remaining four galaxies

**Figure 12.** (Continued.)

becomes 0.82 ± 0.06 , and a Spearman-Rank test yields a 26% probability of being correlated.

We additionally find the de-projected radius at which the observed X-ray source distribution reaches the background level. Beyond this distance, which we denote as r_{bkg} , all observed X-ray sources are likely to be background AGN; within this distance, the observed X-ray sources will be a mix of background AGN and sources intrinsic to the host galaxy

(e.g., XRBs and bright SNRs). Utilizing our sensitivity maps and observed radial source distributions, we estimate the fraction X-ray sources likely to be AGN as a function of de-projected distance from the galaxy (shown by the blue line in Figure 6). The expected AGN contribution as a function of radius is also summarized in Table 11, where for each galaxy (column 1) we list the radii at which we expect AGN to make up $<10\%$ (column 2), $\sim 25\%$ (column 3), $\sim 50\%$ (column 4),

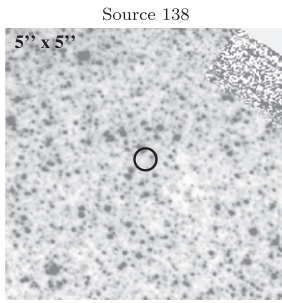


Figure 12. (Continued.)

$\sim 75\%$ (column 5), and 100% (e.g., r_{bkg} ; column 6) of X-ray sources.

5.5. Time Variable Sources

The three X-ray catalogs were systematically searched for sources showing both significant short-term (i.e., that occurs on timescales less than the observation exposure time) and long-term (i.e., occurring over multiple observations spanning months or years) variability in the 0.35–8 keV band. While rapid X-ray variability is routinely observed in both AGN and XRB systems (Vaughan et al. 2003), it is typically not observed in other sources of X-ray emission (i.e., SNRs). Unless otherwise noted, all fluxes or luminosities reported are unabsorbed.

5.5.1. Rapid Variability From Chandra Observations

We used a Kolmogorov–Smirnov (K–S) test to compare the cumulative photon arrival time distribution for each X-ray source to a uniform count rate model in each observation. The K–S test returns the probability (denoted by ξ) that both distributions were drawn from the same parent distribution. We consider sources with $\xi \leq 10^{-3}$ rapidly variable; this value of ξ corresponds to the $\sim 3\sigma$ level.

In NGC 55, we find no sources with K–S probabilities indicative of short-term variability. We find three and four such rapidly varying X-ray sources in NGC 2403 and NGC 4214, respectively. In Figures 8 and 9, we show the cumulative arrival times of photons detected in each exposure for these short-term variable sources. The ξ values of these sources are reported in Table 12.

5.5.2. Long-term Variability From Chandra Observations

To investigate long-term variability of the X-ray sources in each galaxy, we utilize the variability threshold η (as in Tüllmann et al. 2011), defined as $\eta = (\text{flux}_{\text{max}} - \text{flux}_{\text{min}}) / \Delta \text{flux}$, where flux_{max} and flux_{min} are the maximum and minimum fluxes from detections of the source, respectively. The flux error Δflux is calculated using the Gehrels approximation (appropriate for low count data; Gehrels 1986). We consider any sources with $\eta \geq 5$ variable. There are 87 sources in NGC 55, 72 sources in NGC 2403, and 48 sources in NGC 4214 that meet this criterion.

Table 13 provides the long-term Chandra variability η values for sources with $\eta \geq 5$. We additionally list the corresponding maximum to minimum flux ratios for these sources. Column (1) lists the source number. Columns (2) and (3) provide η (indicative of long-term variability), and the ratio

of maximum to minimum observed flux, respectively, for sources in NGC 55. Columns (4) and (5) provide the same information for sources in NGC 2403, and columns (6) and (7) provide the same information for sources in NGC 4214. Only sources showing evidence for variability are included in the table, and these values only refer to variability within or between multiple Chandra observations.

5.5.3. Long-term Variability Using XMM-Newton

In addition to our Chandra survey, multiple archival observations by XMM-Newton are available that contain our catalog sources within the field of view. We utilize XMM-Newton fluxes provided by FLIX,¹¹ an upper limit server for XMM-Newton data provided by the XMM-Newton Survey Science Center. FLIX allows the user to input source coordinates and provides estimates of the flux at the source position, or a flux upper limit where no source was detected, in a variety of energy bands. All fluxes are then converted to the 0.35–8 keV energy band assuming the same spectral model as for our sensitivity maps (a power law with $\Gamma = 1.9$ absorbed by the Galactic column). All XMM-Newton upper limits correspond to the 3σ level.

Tables 14–16 list all available archival X-ray fluxes from both Chandra and XMM-Newton (including upper-limits for exposures during which the source was not detected). For many sources, this included upper limits. The tables follow approximately the same form, with the first column providing the source number. The next several column headings provide the dates on which each Chandra or XMM-Newton observation was performed, listed in chronological order; these columns provide the 0.35–8 keV flux (or 3σ upper limit on the 0.35–8 keV flux) observed in each exposure. The following two columns provide the ratio of the maximum to minimum fluxes, calculated two ways. The first ratio uses only source detections. For some sources, there is a flux upper limit in an observation that is below the faintest source detection; in these cases, we calculate a lower limit on the flux ratio from the lowest measured upper limit.

Figure 10 shows a histogram of these two flux ratios: the ratios derived from source detections only is shown in black, and the ratios found by using a flux upper limit is shown in red. The median flux ratio from detections is ~ 5.8 , while for ratio lower limits it is ~ 8.9 .

X-ray bursting or transient behavior (whereby the flux changes by many orders of magnitude) is observed in both LMXBs and HMXBs (Bozzo et al. 2008; Fragos et al. 2008; Paul & Naik 2011; Revnivtsev et al. 2011). Some of the sources in our catalogs may exhibit such behavior, especially when a source was detected in at least one exposure but not another (despite the source’s position being within the field of view). While previous work on the Antennae has shown the XLFs to be unaffected by such variability (Zezas et al. 2007), these observations only included sources with X-ray luminosities above a few $10^{37} \text{ erg s}^{-1}$ and may not be universal for lower-luminosity sources like those detected in our survey (with luminosities down to $\sim 10^{36} \text{ erg s}^{-1}$).

The heterogeneity of observation exposure times and instruments makes it difficult to identify such transient or bursting sources on an individual basis. When we examine our catalog as a whole, combined with the archival XMM-Newton

¹¹ See: www.ledas.ac.uk/flix/flix.html

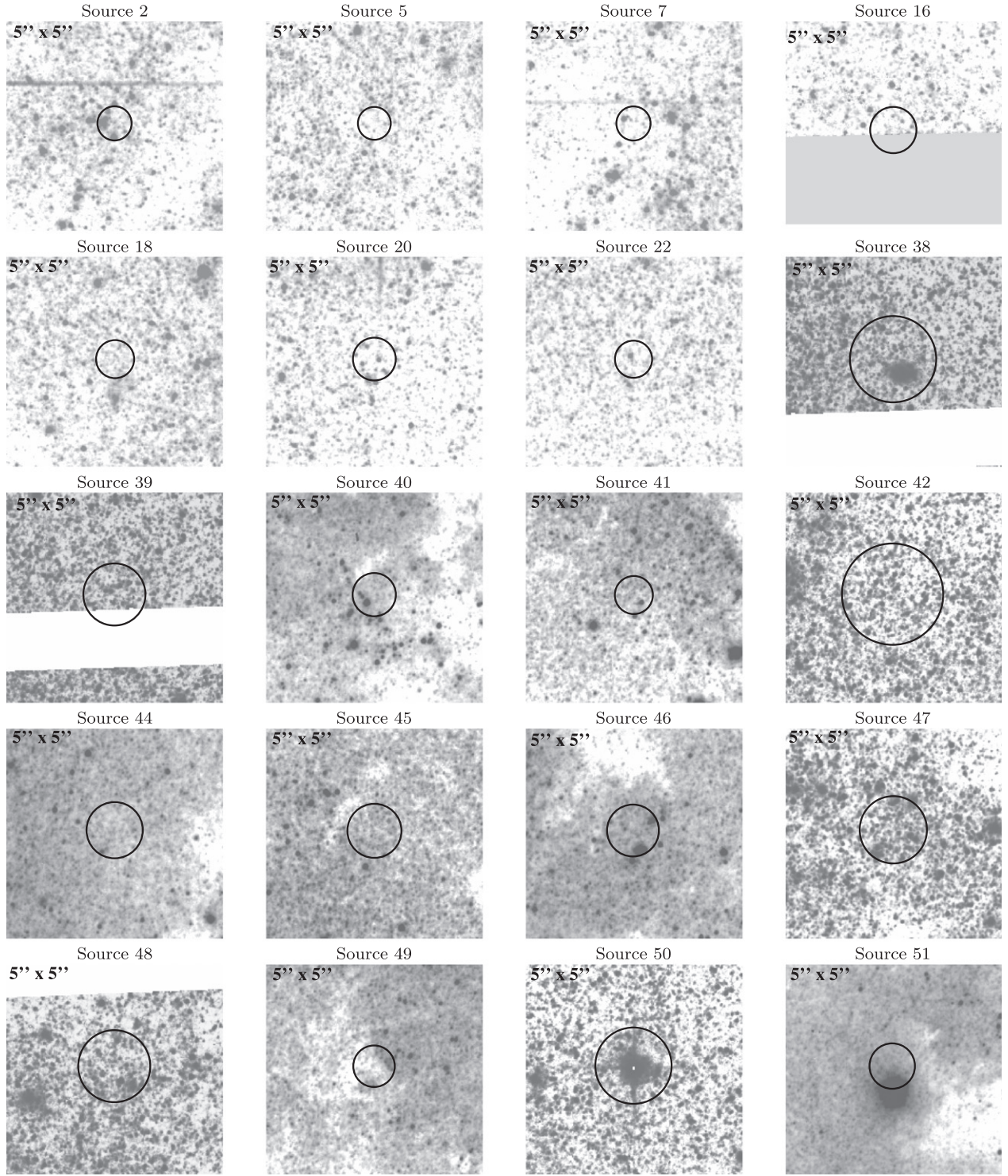


Figure 13. Optical *HST* images for X-ray sources detected in NGC 2403. The box size ($5'' \times 5''$, $10'' \times 10''$, or $15'' \times 15''$) is given in the top-left corner of each image. The circle shows the *Chandra* 90% error circle, centered on the source position.

measurements, we find that $\sim 39\%$ of sources with multiple observations have a maximum-to-minimum flux ratio of at least a factor of ten. The typical flux uncertainty for faint sources ($< 10^{-14} \text{ erg s}^{-1} \text{ cm}^{-2}$) in our catalog is $\sim 30\%$, and the uncertainty decreases to $\sim 5\% - 8\%$ for sources with fluxes $> 10^{-13} \text{ erg s}^{-1} \text{ cm}^{-2}$. For sources with a maximum flux of $< 10^{-14} \text{ erg s}^{-1} \text{ cm}^{-2}$, an order of magnitude decrease in brightness corresponds to a $\sim 3\sigma$ change. For a flux ratio of

~ 10 to be significant at the 5σ level, the maximum flux of the source must exceed $\sim 2 \times 10^{-14} \text{ erg s}^{-1} \text{ cm}^{-2}$. Therefore, only those sources with a maximum flux $> 2 \times 10^{-14} \text{ erg s}^{-1} \text{ cm}^{-2}$ and a flux ratio > 10 are variable at the 5σ level.

When considering the flux ratio lower limits for sources below the detection limit in an observation, we find $\sim 44\%$ of sources show an order of magnitude change or more. However, when only the flux ratios derived from the archival *Chandra*

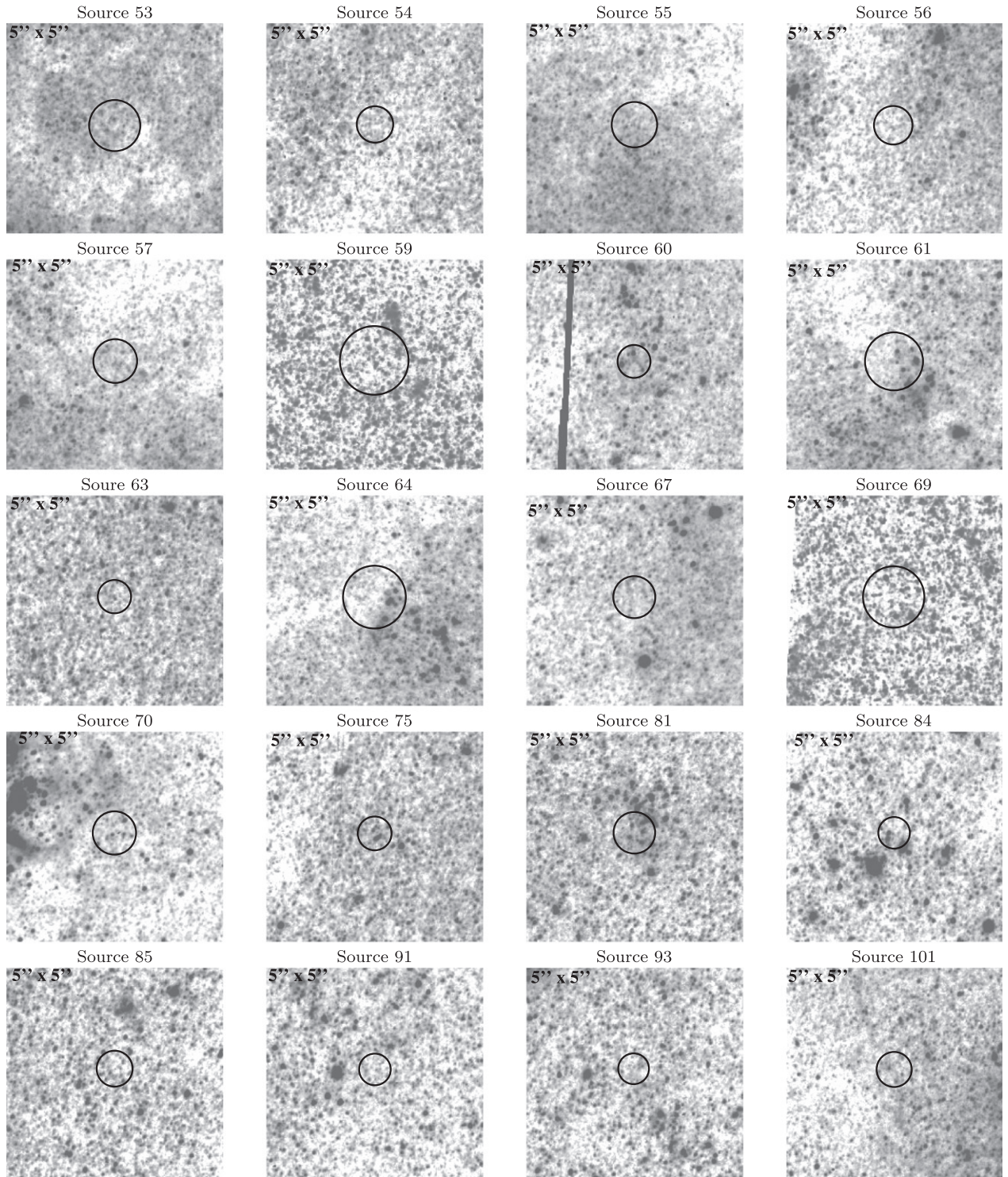


Figure 13. (Continued.)

observations are used, we find only $\sim 16\%$ of sources exhibit a change in flux greater than ten. This suggests that many of these sources with a factor of ~ 10 change in flux is likely due to uncertainties in the flux or detector differences. Only $\sim 11\%$ of sources in our catalog have flux ratios of more than a hundred when all available data is considered, 7% of sources have flux ratios from lower limits of one hundred, and 4% of sources show this level of variability from the *Chandra*-only observations. For these sources, the long-term variability is almost certainly real.

Figure 11 shows the maximum and minimum detected fluxes of source in our catalog as a function of their flux ratio (determined by detections). The flux ratio compared to the minimum flux of each source shows a clear decreasing trend, while the opposite is observed for the same comparison against the maximum flux. These trends are not surprising: in order for a source to have a large flux ratio, it *must* have fluctuated from a relatively low flux to a substantially larger one. For sources with a flux ratio below an order of magnitude there is

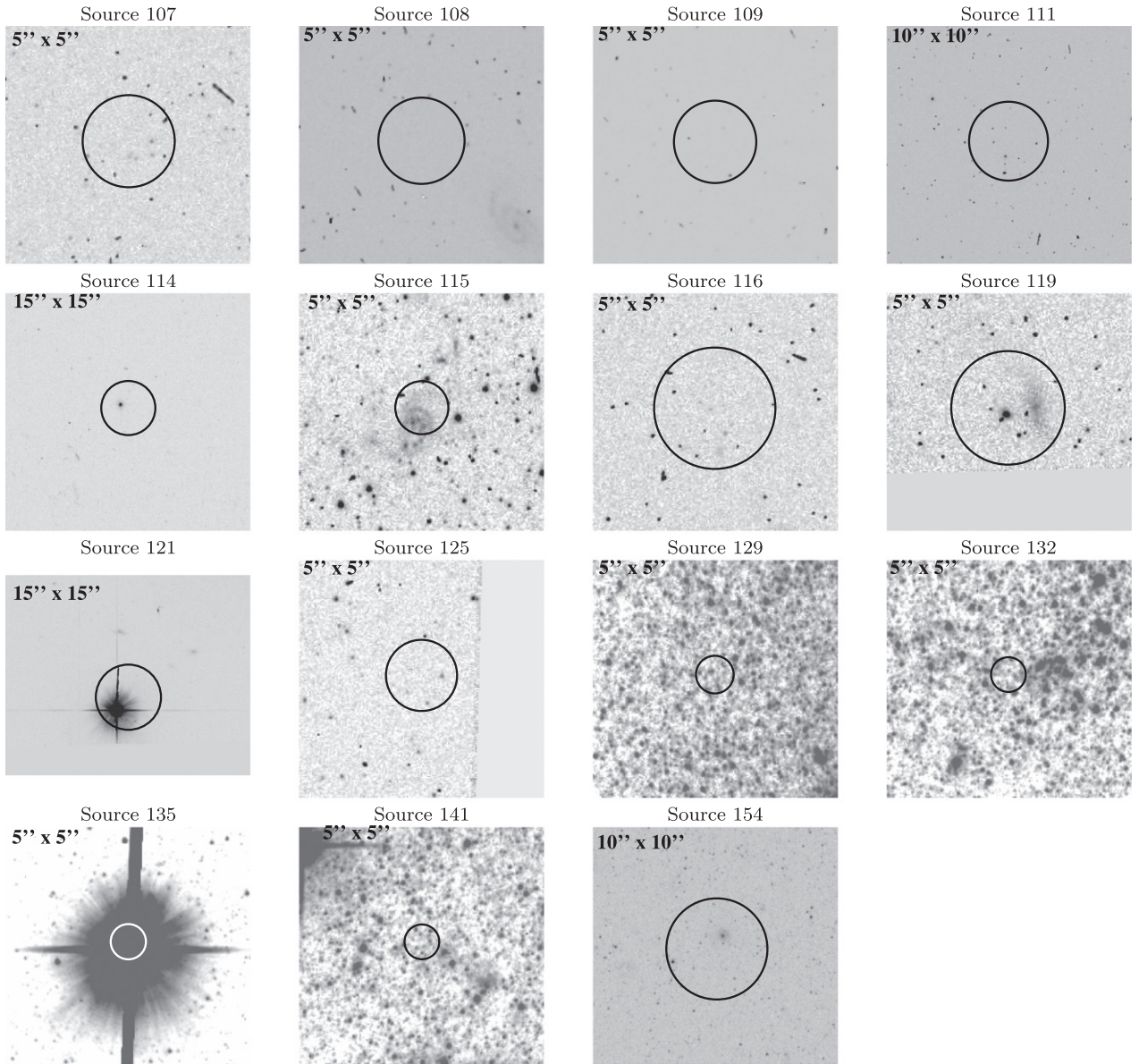


Figure 13. (Continued.)

significant overlap between the minimum and maximum observed fluxes around $\sim 10^{-14}$ erg s $^{-1}$ cm $^{-2}$, revealing the flux range where most of our detections lie.

6. MULTIWAVELENGTH OBSERVATIONS AND SOURCE CLASSIFICATION

6.1. Optical Counterparts from *HST*

To aid in source classification, we searched for optical counterpart candidates for each X-ray source that was contained within one or more of our *HST* fields. For many of our X-ray sources, we found multiple optical counterpart candidates within the *Chandra* X-ray error circle (typically, with radii on the order of $\sim 0''.5$). We kept only those optical sources that met the quality cuts described in Williams et al. (2009): i.e., sources with a sufficiently high signal-to-noise ratio, not flagged as unusable, meeting predetermined crowding

and sharpness thresholds, etc. The *HST* exposures reach a typical limiting magnitude of 26 in *F814W* and 27 in *F606W*, making late B-type main sequence stars (and in some cases, early A-type main sequence stars) detectable in our observations. Figures 12–14 show “postage stamp” finding charts for each X-ray source covered by an *HST* pointing. The 90% *Chandra* positional uncertainty, centered on the source position, is indicated in the figures.

To determine the likely source classification, we utilized color–magnitude diagrams (CMDs) and X-ray color–magnitude diagrams (XCMDs) as in Paper I. We provide a brief summary of our approach here, and the reader is referred to Paper I for further details. We use the optical colors from our *HST* observations to separate optical counterpart candidates into main sequence (“MS”; our exposures are sensitive to A-type stars and earlier) or red giant branch subgroups. Many authors have shown it is possible to use a combination of X-ray and optical

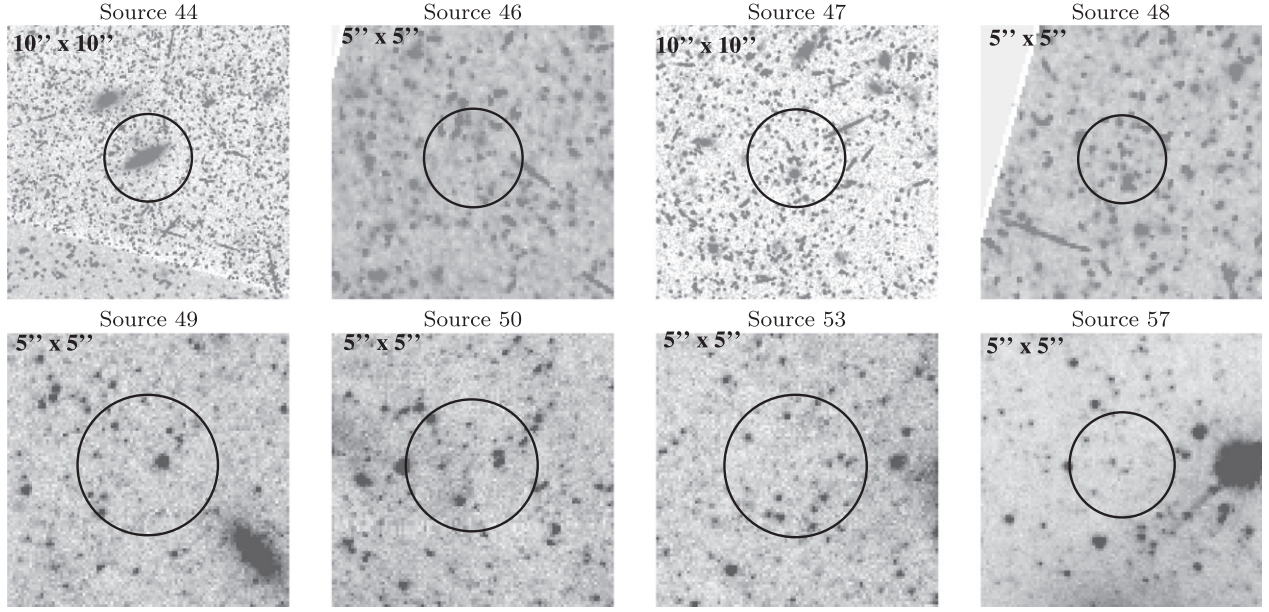


Figure 14. Optical *HST* images for X-ray sources detected in NGC 4214. The box size ($5'' \times 5''$, $10'' \times 10''$, or $15'' \times 15''$) is given in the top-left corner of each image. The circle shows the *Chandra* 90% error circle, centered on the source position.

Table 17
Public Multiwavelength Data for NGC 55 X-ray Sources

Source	# <i>HST</i>	SIMBAD	USNO-B1.0					2MASS			GALEX	
No.	Matches	ID ^a	B1	R1	B2	R2	I	J	H	K	FUV	NUV
(1)	(2)	(3)	(4)	(5)	(6)	(7)	(8)	(9)	(10)	(11)	(12)	(13)
1	19.40	...
2	19.88	17.83	22.24	21.28
3	24.18	23.41
5	22.66
7	<i>ROSAT</i>	19.93	20.45	23.47	23.29	20.25
8	20.17	20.22	20.55	22.31
10	16.47	...
11	21.67	...
12	23.44	22.82
13	21.88	22.66

Note.

^a SIMBAD counterparts are listed as: SNR (supernova remnant), radio (radio source), H II (H II region), galaxy, Cl* (star cluster), QSO, SN (supernova designation), star, ULX, *ROSAT* (historically known *ROSAT* source), *EINSTEIN* (historically known *Einstein* source), GC (globular cluster), cepheid, em. gal (emission-line galaxy), gal. group (galaxy group), RS CVN (cataclysmic variable).

(This table is available in its entirety in machine-readable and Virtual Observatory (VO) forms.)

colors to discriminate between XRBs and background AGN (e.g., Hornschemeier et al. 2001; Shtykovskiy & Gilfanov 2005).

McGowan et al. (2008) found that known pulsars and HMXBs located in the Small Magellanic Cloud occupied a region of the XCMD defined by a combination of optical colors and X-ray-to-optical flux ratio. In order to directly compare with HMXBs in the SMC, we use their definition of the logarithmic X-ray-to-optical flux ratio, $\log(f_X/f_V)$, where f_X is the 2–10 keV flux and f_V is the optical flux. We compute this flux ratio for each source within the error circle, using the observed flux in either *F555W* or *F606W* for the *V*-band, whichever is available. Although the *F606W* filter has a larger bandpass than *F555W*, we estimate that for the majority of stars accessible in our *HST* exposures the effect on $\log(f_X/f_V)$ will be small, ~ 0.1 . To estimate the 2–10 keV flux, we convert

the measured 2–8 keV to the 2–10 keV energy band using WebPIMMs¹² and the best-fit spectral model (for sufficiently bright sources) or the assumed power law with Galactic absorption used in our sensitivity map computation.

The region of the XCMD bounded by $B - V \lesssim 0$ and $\log(f_X/f_V) \lesssim 1$ contains likely pulsars and HMXBs, while LMXBs and AGN preferentially fall outside this region. We therefore separate the candidate optical counterparts into likely “AGN” or “HMXB” subgroups. If *any* of the optical counterpart candidates is consistent with the HMXB subgroup, we classify the X-ray source as an HMXB candidate; otherwise, the source is placed into a different category (e.g., an AGN).

¹² See <http://heasarc.gsfc.nasa.gov/cgi-bin/Tools/w3pimms/w3pimms.pl>.

Table 18
Public Multiwavelength Data for NGC 2403 X-ray Sources

Source	# <i>HST</i>	SIMBAD	USNO-B1.0					2MASS			GALEX	
No.	Matches	ID ^a	<i>B</i> 1	<i>R</i> 1	<i>B</i> 2	<i>R</i> 2	<i>I</i>	<i>J</i>	<i>H</i>	<i>K</i>	FUV	NUV
(1)	(2)	(3)	(4)	(5)	(6)	(7)	(8)	(9)	(10)	(11)	(12)	(13)
1	21.03	21.02
2	2
3	17.47	17.32
5	3
7	11	16.01	15.80
9	20.92	19.01
11	23.46	22.37
12	20.85	20.06
13
14	20.99	...	21.77	23.48	22.83

Note.

^a SIMBAD counterparts are listed as: SNR (supernova remnant), radio (radio source), H II (H II region), galaxy, Cl* (star cluster), QSO, SN (supernova designation), star, ULX, *ROSAT* (historically known *ROSAT* source), *EINSTEIN* (historically known *Einstein* source), GC (globular cluster), cepheid, em. gal (emission-line galaxy), gal. group (galaxy group), RS CVN (cataclysmic variable).

(This table is available in its entirety in machine-readable and Virtual Observatory (VO) forms.)

6.2. Comparisons with Multiwavelength Catalogs

We have also attempted to place constraints on the nature of the X-ray sources contained in the CLVS catalogs by examining archival multi-wavelength data. We searched for counterparts in the following point source catalogs: the *GALEX* GR6 data release (NUV, FUV), USNO-B1.0 (*B*, *R*), 2MASS All Sky (*J*, *H*, *K*), and NVSS (1.4 GHz). X-ray source positions were also correlated with SIMBAD objects. Tables 17–19 summarize the multiwavelength observations available for each of the X-ray sources with at least one multi-wavelength detection. All three tables follow approximately the same format, with column (1) providing the source number. Column (2) provides the number of potential optical *HST* sources falling within the *Chandra* error circle. Column (3) provides the identifying information from the SIMBAD catalog. The next several columns provide the magnitudes of multiwavelength counterparts from a variety of public source catalogs: USNO-B1.0, SDSS, 2MASS, and *GALEX*.

UV emission can be a good tracer of young stars and background AGN. It is possible that some LMXBs will additionally exhibit detectable levels of UV emission, although their optical colors are expected to be significantly redder than those of an AGN. The optical USNO-B1.0 catalog provides photometric data for objects in five optical bandpasses and provides a ~85% accuracy for distinguishing foreground Milky Way stars from non-stellar objects (Monet et al. 2003), making it possible to separate these sources from clusters and nearby AGN. The infrared data are also sensitive to Milky Way stars, red giants, associations of older stars, and background galaxies. Radio emission is indicative of radio-loud background AGN; however, a large fraction of AGN are known to be radio-quiet (Kellermann et al. 1989), so the lack of radio emission is not used to disqualify an AGN origin for a given X-ray source. Although many SNRs, both Galactic and in nearby galaxies have been detected at radio frequencies, most have too low a radio surface brightness to be detectable at distances of a few Mpc (e.g., Gordon et al. 1999; Long et al. 2010).

6.3. Source Classification

We combine all of the X-ray and multi-wavelength data available for each source to determine a likely source classification. While the detection of optical counterpart candidates for those X-ray sources with overlapping *HST* fields allows some sources to be assigned a classification based on their multiwavelength properties, many X-ray sources are faint or do not have optical coverage, making their physical nature ambiguous. We therefore attempt to additionally combine statistical quantities (i.e., using the radial source distribution, location in spiral arms, inter-arm regions, or background regions) with individual source properties (variability, X-ray spectral shape, and optical colors) to determine the most likely source classification. For a fair comparison with the NGC 300 X-ray source catalog (see Paper I for details), we use the `xclass` IDL routine¹³ to carry out our final source classifications. Since the primary goal of the CLVS is to study the HMXB populations of these galaxies, the `xclass` classifier was designed to quickly find sources with properties consistent with HMXBs (e.g., blue optical counterpart, associated with spiral arms, X-ray spectrum or hardness most consistent with a power law $\Gamma \sim 0.5\text{--}2.5$, etc.). Some X-ray sources that are not classified as HMXBs (most of which are then classified as AGN) will undoubtedly possess individually interesting properties; thus, some users may decide to perform a follow-up analysis on a different output category.

The final source classifications for NGC 55, NGC 2403, and NGC 4214 are displayed in Figure 15 and are summarized in Table 20. Column (1) lists the source number. Column (2) provides the preliminary source classification based on the HRs alone. Column (3) lists the galactocentric distance of the source (in kpc). Column (4) lists whether or not the source appears associated with the galaxy (i.e., coincident with a spiral arm). Column (5) lists whether evidence for X-ray variability was observed and, if so, what type (“rapid” and/or “long”). Column (6) lists whether the source had its X-ray spectrum fit and, if so,

¹³ See <http://www.astro.washington.edu/users/bbinder/xclass/>

Table 19
Public Multiwavelength Data for NGC 4214 Sources

Source	<i>HST</i>	SIMBAD	USNO-B1.0					SDSS					2MASS			GALEX	
No.	Matches	ID	<i>B</i> 1	<i>R</i> 1	<i>B</i> 2	<i>R</i> 2	<i>I</i>	<i>u</i>	<i>g</i>	<i>r</i>	<i>i</i>	<i>z</i>	<i>J</i>	<i>H</i>	<i>K</i>	FUV	NUV
(1)	(2)	(3)	(4)	(5)	(6)	(7)	(8)	(9)	(10)	(11)	(12)	(13)	(14)	(15)	(16)	(17)	(18)
1	18.25	19.79	...	19.46	...	22.25	22.28	21.79	22.47	22.59
2	22.97	23.68	23.64	22.37	20.15
3	22.44	22.72	23.05	21.62	21.70	22.64
4	24.34
5	19.47	20.59	19.44	17.21	23.11	20.81	19.31	17.86	17.08	15.83	15.12	14.60	20.15	...
6	23.14	22.86	22.18	21.64	21.32	23.53
8	21.32
10	19.91	18.63
13	20.25	20.25	20.76	...	20.57	20.54	20.54	20.15	20.23	22.65	21.79
14	21.82	21.41	21.12	20.62	20.25	21.99

Note.
^a SIMBAD counterparts are listed as: SNR (supernova remnant), radio (radio source), H II (H II region), galaxy, Cl* (star cluster), QSO, SN (supernova designation), star, ULX, *ROSAT* (historically known *ROSAT* source), *EINSTEIN* (historically known *Einstein* source), GC (globular cluster), cepheid, em. gal (emission-line galaxy), gal. group (galaxy group), RS CVN (cataclysmic variable).
 (This table is available in its entirety in machine-readable and Virtual Observatory (VO) forms.)

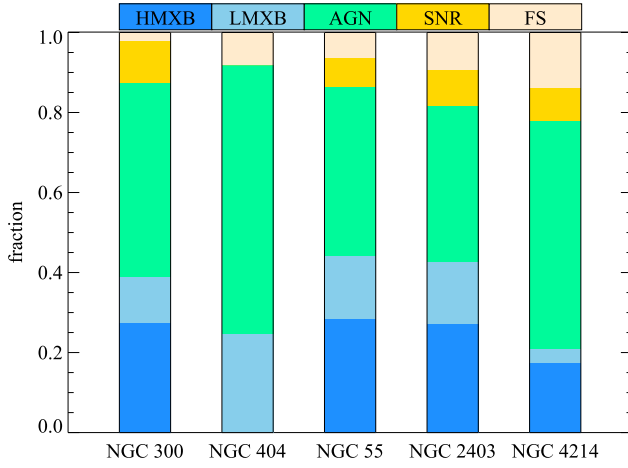


Figure 15. The fraction of X-ray sources classified as HMXBs, LMXBs, background AGN, foreground stars (“FS”), and SNRs in each galaxy.

what general shape the spectrum showed (“po,” “diskbb,” etc.). Column (7) provides the source type as determined by the X-ray to optical flux ratio. Column (8) summarizes what publicly available multiwavelength information is available for the source. Column (9) lists any known counterparts to the source (e.g., foreground star, SNR, etc.) from SIMBAD. Column (10) lists our final classification of the source based on all available data.

7. SUMMARY

We have constructed comprehensive X-ray point source catalogs of NGC 55, NGC 2403, and NGC 4214 as part of the CLVS. When combined with the catalogs of NGC 300 (Binder et al. 2012) and NGC 404 (Binder et al. 2013), the CLVS contains 629 X-ray sources down to a limiting unabsorbed luminosity of $\sim 5 \times 10^{35} \text{ erg s}^{-1}$ in the 0.35–8 keV band. We have presented X-ray HRs, spectral analysis, radial source

Table 20
Final X-ray Source Classification

Source No.	Class from HRs	d (kpc)	Assoc. with Galaxy?	Variability	X-ray Spectrum	f_x/f_o Class	Multi-wavelength	Known Counterpart ^a	Final Classification
(1)	(2)	(3)	(4)	(5)	(6)	(7)	(8)	(9)	(10)
NGC 55									
1	XRB	2.3	FUV	...	AGN
2	ABS	3.0	...	long	optical, FUV, NUV	...	AGN
3	XRB	6.3	...	long	po	...	FUV, NUV	...	AGN
4	XRB	4.4	AGN
5	ABS	3.2	NUV	...	AGN
6	ABS	0.6	✓	long	HMXB
7	SOFT	7.6	po	...	optical, FUV, NUV	ROSAT	AGN
8	ABS	6.4	po	...	optical, NUV	...	AGN
9	XRB	2.3	AGN
10	XRB	0.2	✓	long	FUV	...	LMXB?
NGC 2403									
1	XRB	0.5	FUV, NUV	...	AGN
2	XRB	1.4	✓	rapid	po+2apcc	AGN	LMXB
3	SOFT	3.1	✓	long	po	...	FUV, NUV	...	LMXB?
4	ABS	1.7	...	long	AGN
5	XRB	1.0	✓	AGN	LMXB
6	SNR	2.8	✓	HMXB
7	ABS	1.3	✓	long	...	AGN	FUV, NUV	...	LMXB
8	ABS	3.5	✓	HMXB
9	XRB	4.9	diskbb	...	FUV, NUV	...	AGN
10	XRB	0.8	✓	HMXB
NGC 4214									
1	SNR	0.8	optical	...	star?
2	XRB	1.5	...	long	optical	...	AGN
3	XRB	1.8	...	long	optical	...	AGN
4	XRB	0.0	NUV	...	AGN
5	SNR	0.6	optical, FUV	...	star?
6	XRB	0.6	optical, NUV	...	AGN
7	XRB	1.2	✓	HMXB
8	XRB	0.8	NUV	...	AGN
9	ABS	0.6	AGN
10	HARD	1.5	✓	long	optical	...	LMXB

Note.

^a SIMBAD counterparts are listed as: SNR (supernova remnant), radio (radio source), H II (H II region), galaxy, Cl* (star cluster), QSO, SN (supernova designation), star, ULX, ROSAT (historically known *ROSAT* source), *EINSTEIN* (historically known *Einstein* source), GC (globular cluster), cepheid, em. gal (emission-line galaxy), gal. group (galaxy group), RS CVN (cataclysmic variable).

(This table is available in its entirety in machine-readable and Virtual Observatory (VO) forms.)

distributions, and an analysis of the temporal variability for the X-ray sources detected in NGC 55, NGC 2403, and NGC 4214. To constrain the nature of each X-ray source, cross-correlations with multi-wavelength data were generated, and we searched overlapping *HST* fields for optical counterparts to our X-ray detections. Based on all of this information, each X-ray source was classified as a candidate XRB, background AGN, SNR, or foreground star. The catalogs constructed for the CLVS will be used in a follow-up paper analyze the properties of the source populations in more depth, discuss the implications of our data for scenarios of HMXB evolution and to make connections between those populations and to the morphology, SFH, and metallicity of the host galaxy.

We would like to thank the anonymous referee for the helpful comments and recommendations that improved this manuscript. B. B. and B. F. W. acknowledge support from *Chandra* grant AR2-13005X. T. J. G. and P. P. P. acknowledge support under NASA contract NAS8-03060 with the *Chandra* X-ray Center. This research has made use of the NASA/IPAC Extragalactic Database (NED) which is operated by the Jet Propulsion Laboratory, California Institute of Technology, under contract with the National Aeronautics and Space Administration. This research has made use of the VizieR catalog access tool, CDS, Strasbourg, France. The original description of the VizieR service was published in A&AS, 143, 23

REFERENCES

- Agüeros, M. A., Anderson, S. F., Covey, K. R., et al. 2009, *ApJS*, **181**, 444
- Arnaud, K. A. 1996, in ASP Conf. Ser. 101, *Astronomical Data Analysis Software and Systems V*, ed. G. H. Jacoby & J. Barnes (San Francisco, CA: ASP), 17
- Arnaud, K. A., Smith, R. K., Siemiginowska, A., et al. 2011, *Handbook of X-Ray Astronomy* (Cambridge: Cambridge Univ. Press)
- Baggett, W. E., Baggett, S. M., & Anderson, K. S. J. 1998, *AJ*, **116**, 1626
- Barker, M. K., Ferguson, A. M. N., Irwin, M. J., Arimoto, N., & Jablonka, P. 2012, *MNRAS*, **419**, 1489
- Belczynski, K., Kalogera, V., Zezas, A., & Fabbiano, G. 2004, *ApJL*, **601**, L147
- Berg, D. A., Skillman, E. D., Garnett, D. R., et al. 2013, *ApJ*, **775**, 128
- Beswick, R. J., Muxlow, T. W. B., Argo, M. K., et al. 2005, *ApJL*, **623**, L21
- Binder, B., Williams, B. F., Eracleous, M., et al. 2012, *ApJ*, **758**, 15
- Binder, B., Williams, B. F., Eracleous, M., et al. 2013, *ApJ*, **763**, 128
- Bozzo, E., Falanga, M., & Stella, L. 2008, *ApJ*, **683**, 1031
- Bresolin, F. 2013, *ApJL*, **772**, L23
- Bresolin, F., Gieren, W., Kudritzki, R.-P., et al. 2009, *ApJ*, **700**, 309
- Broos, P. S., Townsley, L. K., Feigelson, E. D., et al. 2010, *ApJ*, **714**, 1582
- Cappelluti, N., Brusa, M., Hasinger, G., et al. 2009, *A&A*, **497**, 635
- Cash, W. 1979, *ApJ*, **228**, 939
- Chakraborti, S., Yadav, N., Ray, A., et al. 2012, *ApJ*, **761**, 100
- Dahlem, M., Weaver, K. A., & Heckman, T. M. 1998, *ApJS*, **118**, 401
- Dahm, S. E., Simon, T., Proszkow, E. M., & Patten, B. M. 2007, *AJ*, **134**, 999
- Dalcanton, J. J., Williams, B. F., Seth, A. C., et al. 2009, *ApJS*, **183**, 67
- Davidge, T. J., & Courteau, S. 2002, *AJ*, **123**, 1438
- Davis, J. E. 2001, *ApJ*, **562**, 575
- de Blok, W. J. G., Walter, F., Brinks, E., et al. 2008, *AJ*, **136**, 2648
- de Vaucouleurs, G. 1961, *ApJ*, **133**, 405
- de Vaucouleurs, G., de Vaucouleurs, A., Corwin, H. G., Jr., et al. 1991, *Third Reference Catalogue of Bright Galaxies* (New York: Springer)
- Dewi, J. D. M. 2006, *MNRAS*, **372**, L1
- Drissen, L., Roy, J.-R., Moffat, A. F. J., & Shara, M. M. 1999, *AJ*, **117**, 1249
- Engelbracht, C. W., Gordon, K. D., Bendo, G. J., et al. 2004, *ApJS*, **154**, 248
- Engelbracht, C. W., Rieke, G. H., Gordon, K. D., et al. 2008, *ApJ*, **678**, 804
- Eracleous, M., Sipior, M. S., & Sigurdsson, S. 2006, in IAU Symp. 230, *Populations of High Energy Sources in Galaxies*, ed. E. J. A. Meurs & G. Fabbiano (Cambridge: Cambridge Univ. Press), 417
- Fabbiano, G. 2006, *ARA&A*, **44**, 323
- Fabbiano, G., & Trinchieri, G. 1987, *ApJ*, **315**, 46
- Fabbiano, G., & White, N. E. 2006, in *Compact Stellar X-ray Sources in Normal Galaxies*, ed. W. H. G. Lewin & M. van der Klis (Cambridge: Cambridge Univ. Press), 475
- Feng, H., & Kaaret, P. 2005, *ApJ*, **633**, 1052
- Ferguson, A. M. N., Wyse, R. F. G., & Gallagher, J. S. 1996, *AJ*, **112**, 2567
- Fragos, T., Kalogera, V., Belczynski, K., et al. 2008, *ApJ*, **683**, 346
- Fraternali, F., Cappi, M., Sancisi, R., & Oosterloo, T. 2002, *ApJ*, **578**, 109
- Freedman, W. L., & Madore, B. F. 1988, *ApJL*, **332**, L63
- Freeman, P. E., Kashyap, V., Rosner, R., & Lamb, D. Q. 2002, *ApJS*, **138**, 185
- Gehrels, N. 1986, *ApJ*, **303**, 336
- Georgakakis, A., Nandra, K., Laird, E. S., Aird, J., & Trichas, M. 2008, *MNRAS*, **388**, 1205
- Ghosh, K. K., Rappaport, S., Tennant, A. F., et al. 2006, *ApJ*, **650**, 872
- Gilfanov, M., Grimm, H.-J., & Sunyaev, R. 2004, *MNRAS*, **347**, L57
- Gordon, S. M., Duric, N., Kirshner, R. P., Goss, W. M., & Viallefond, F. 1999, *ApJS*, **120**, 247
- Grimm, H.-J., Gilfanov, M., & Sunyaev, R. 2003, *MNRAS*, **339**, 793
- Hartwell, J. M., Stevens, I. R., Strickland, D. K., Heckman, T. M., & Summers, L. K. 2004, *MNRAS*, **348**, 406
- Heida, M., Jonker, P. G., Torres, M. A. P., et al. 2013, *MNRAS*, **433**, 681
- Hoopes, C. G., Walterbos, R. A. M., & Greenwalt, B. E. 1996, *AJ*, **112**, 1429
- Hornschemeier, A. E., Brandt, W. N., Garmire, G. P., et al. 2001, *ApJ*, **554**, 742
- Huchra, J. P., Geller, M. J., Gallagher, J., et al. 1983, *ApJ*, **274**, 125
- Humphrey, P. J., Liu, W., & Buote, D. A. 2009, *ApJ*, **693**, 822
- Humphreys, R. M., Prieto, J. L., Rosenfield, P., et al. 2010, *ApJL*, **718**, L43
- Hunsch, M., Schmitt, J. H. M. M., & Voges, W. 1998, *A&AS*, **127**, 251
- Isobe, N., Makishima, K., Takahashi, H., et al. 2009, *PASJ*, **61**, 279
- Kalberla, P. M. W., Burton, W. B., Hartmann, D., et al. 2005, *A&A*, **440**, 775
- Karachentsev, I. D., Dolphin, A. E., Geisler, D., et al. 2002, *A&A*, **383**, 125
- Karachentsev, I. D., Karachentseva, V. E., Huchtmeier, W. K., & Makarov, D. I. 2004, *AJ*, **127**, 2031
- Kellermann, K. I., Sramek, R., Schmidt, M., Shaffer, D. B., & Green, R. 1989, *AJ*, **98**, 1195
- Kennicutt, R. C., Jr. 1998, *ARA&A*, **36**, 189
- Kilgard, R. E., Cowan, J. J., Garcia, M. R., et al. 2005, *ApJS*, **159**, 214
- Komossa, S., Böhringer, H., & Huchra, J. P. 1999, *A&A*, **349**, 88
- Kong, A. K. H., & Di Stefano, R. 2003, *ApJL*, **590**, L13
- Kong, A. K. H., Garcia, M. R., Primini, F. A., et al. 2002, *ApJ*, **577**, 738
- Kotoku, J., Mizuno, T., Kubota, A., & Makishima, K. 2000, *PASJ*, **52**, 1081
- Kuulkers, E., Norton, A., Schwope, A., & Warner, B. 2006, in *Compact Stellar X-Ray Sources*, ed. W. H. G. Lewin & M. van der Klis (Cambridge: Cambridge Univ. Press), 475
- Lee, H., Skillman, E. D., Cannon, J. M., et al. 2006, *ApJ*, **647**, 970
- Long, K. S., Blair, W. P., Winkler, P. F., et al. 2010, *ApJS*, **187**, 495
- Maíz-Apellániz, J., Bond, H. E., Siegel, M. H., et al. 2004, *ApJL*, **615**, L113
- Maíz-Apellániz, J., Cieza, L., & MacKenty, J. W. 2002, *AJ*, **123**, 1307
- Makishima, K., Kubota, A., Mizuno, T., et al. 2000, *ApJ*, **535**, 632
- Makishima, K., Maejima, Y., Mitsuda, K., et al. 1986, *ApJ*, **308**, 635
- Masetti, N., Orlandini, M., Palazzi, E., Amati, L., & Frontera, F. 2006, *A&A*, **453**, 295
- Matonick, D. M., Fesen, R. A., Blair, W. P., & Long, K. S. 1997, *ApJS*, **113**, 333
- McClintock, J. E., & Remillard, R. A. 2006, in *Compact Stellar X-Ray Sources*, ed. W. H. G. Lewin & M. van der Klis (Cambridge: Cambridge Univ. Press), 421
- McGowan, K. E., Coe, M. J., Schurch, M. P. E., et al. 2008, *MNRAS*, **383**, 330
- Micela, G., Sciortino, S., Kashyap, V., Harnden, F. R., Jr., & Rosner, R. 1996, *ApJS*, **102**, 75
- Mineo, S., Gilfanov, M., & Sunyaev, R. 2011, *AN*, **332**, 349
- Mineo, S., Gilfanov, M., & Sunyaev, R. 2012, *MNRAS*, **419**, 2095
- Monet, D. G., Levine, S. E., Canzian, B., et al. 2003, *AJ*, **125**, 984
- Muñoz-Mateos, J. C., Gil de Paz, A., Boissier, S., et al. 2007, *ApJ*, **658**, 1006
- Nakano, S., & Itagaki, K. 2004, *CBET*, **74**, 1
- Nandra, K., Laird, E. S., Adelberger, K., et al. 2005, *MNRAS*, **356**, 568
- Nousek, J. A., & Shue, D. R. 1989, *ApJ*, **342**, 1207
- Ott, J., Walter, F., & Brinks, E. 2005, *MNRAS*, **358**, 1453
- Otte, B., & Dettmar, R.-J. 1999, *A&A*, **343**, 705
- Park, T., Kashyap, V. L., Siemiginowska, A., et al. 2006, *ApJ*, **652**, 610
- Paul, B., & Naik, S. 2011, *BASI*, **39**, 429
- Pickles, A., & Depagne, É. 2010, *PASP*, **122**, 1437
- Plucinsky, P. P., Williams, B., Long, K. S., et al. 2008, *ApJS*, **174**, 366
- Prestwich, A. H., Irwin, J. A., Kilgard, R. E., et al. 2003, *ApJ*, **595**, 719
- Prosser, C. F., Randich, S., Stauffer, J. R., Schmitt, J. H. M. M., & Simon, T. 1996, *AJ*, **112**, 1570
- Puche, D., Carignan, C., & Bosma, A. 1990, *AJ*, **100**, 1468

- Puche, D., Carignan, C., & Wainscoat, R. J. 1991, [AJ](#), **101**, 447
- Read, A. M., Ponman, T. J., & Strickland, D. K. 1997, [MNRAS](#), **286**, 626
- Revnivtsev, M., Postnov, K., Kuranov, A., & Ritter, H. 2011, [A&A](#), **526**, A94
- Robinson, B. J., & van Damme, K. J. 1966, [AuJPh](#), **19**, 111
- Salpeter, E. E. 1955, [ApJ](#), **121**, 161
- Sargent, W. L. W., & Filippenko, A. V. 1991, [AJ](#), **102**, 107
- Schlegel, E. M., Barrett, P., & Singh, K. P. 1997, [AJ](#), **113**, 1296
- Schlegel, E. M., & Pannuti, T. G. 2003, [AJ](#), **125**, 3025
- Schmidt, K.-H., & Boller, T. 1993, [AN](#), **314**, 361
- Seth, A. C., Dalcanton, J. J., & de Jong, R. S. 2005, [AJ](#), **129**, 1331
- Shtykovskiy, P., & Gilfanov, M. 2005, [MNRAS](#), **362**, 879
- Shtykovskiy, P. E., & Gilfanov, M. R. 2007, [AstrL](#), **33**, 437
- Skrutskie, M. F., Cutri, R. M., Stiening, R., et al. 2006, [AJ](#), **131**, 1163
- Soria, R., & Kong, A. K. H. 2002, [ApJL](#), **572**, L33
- Stiele, H., Pietsch, W., Haberl, F., et al. 2011, [A&A](#), **534**, A55
- Stobbat, A.-M., Roberts, T. P., & Warwick, R. S. 2004, [MNRAS](#), **351**, 1063
- Stobbat, A.-M., Roberts, T. P., & Warwick, R. S. 2006a, [MNRAS](#), **370**, 25
- Stobbat, A.-M., Roberts, T. P., & Wilms, J. 2006b, [MNRAS](#), **368**, 397
- Swartz, D. A., Ghosh, K. K., Tennant, A. F., & Wu, K. 2004, [ApJS](#), **154**, 519
- Thilker, D. A., Bianchi, L., Schiminovich, D., et al. 2010, [ApJL](#), **714**, L171
- Tikhonov, N. A., Galazutdinova, O. A., & Drozdovsky, I. O. 2005, [A&A](#), **431**, 127
- Trudolyubov, S. P., Borozdin, K. N., Priedhorsky, W. C., Mason, K. O., & Cordova, F. A. 2002, [ApJL](#), **571**, L17
- Tüllmann, R., Gaetz, T. J., Plucinsky, P. P., et al. 2011, [ApJS](#), **193**, 31
- Tüllmann, R., & Rosa, M. R. 2004, [A&A](#), **416**, 243
- Tüllmann, R., Rosa, M. R., Elwert, T., et al. 2003, [A&A](#), **412**, 69
- Úbeda, L., Maíz-Apellániz, J., & MacKenty, J. W. 2007a, [AJ](#), **133**, 917
- Úbeda, L., Maíz-Apellániz, J., & MacKenty, J. W. 2007b, [AJ](#), **133**, 932
- van den Berg, M., Hong, J. S., & Grindlay, J. E. 2009, [ApJ](#), **700**, 1702
- Vaughan, S., Edelson, R., Warwick, R. S., & Uttley, P. 2003, [MNRAS](#), **345**, 1271
- Vinkó, J., Takats, K., Sárneczky, K., et al. 2006, [MNRAS](#), **369**, 1780
- Wang, X., Yang, Y., Zhang, T., et al. 2005, [ApJL](#), **626**, L89
- Weisskopf, M. C., Wu, K., Trimble, V., et al. 2007, [ApJ](#), **657**, 1026
- Wellmann, P. 1955, [ZA](#), **35**, 205
- Williams, B. F., Dalcanton, J. J., Dolphin, A. E., Holtzman, J., & Sarajedini, A. 2009, [ApJL](#), **695**, L15
- Williams, B. F., Dalcanton, J. J., Gilbert, K. M., et al. 2010, [ApJ](#), **716**, 71
- Williams, B. F., Dalcanton, J. J., Gilbert, K. M., et al. 2011, [ApJ](#), **735**, 22
- Williams, B. F., Dalcanton, J. J., Stilp, A., et al. 2013, [ApJ](#), **765**, 120
- Williams, B. F., Gaetz, T. J., Haberl, F., et al. 2008, [ApJ](#), **680**, 1120
- Williams, B. F., Garcia, M. R., Kong, A. K. H., et al. 2004, [ApJ](#), **609**, 735
- Yamaoka, H. 2004, [IAUC](#), **8385**, 1
- Yukita, M., Swartz, D. A., Soria, R., & Tennant, A. F. 2007, [ApJ](#), **664**, 277
- Zang, Z., Warwick, R. S., & Meurs, E. J. A. 1997, [IrAJ](#), **24**, 45
- Zezas, A., Fabbiano, G., Baldi, A., et al. 2007, [ApJ](#), **661**, 135